Appendix I.

Cooling water dispersion modelling study (RPS 2017b)

ConocoPhillips Barossa Project

Cooling Water Dispersion Modelling

Prepared by:

RPS

Suite E1, Level 4
140 Bundall Rd
Bundall, QLD 4217

T: +61 7 5574 1112
F: +61 8 9211 1122
E: szigic@pasa.com.au

Client Manager: Dr Sasha Zigic
Report Number: MAQ0540J.000
Version / Date: Rev2/7 March 2017

Prepared for:

CONOCOPHILLIPS AUSTRALIA

Dr Brenton Chatfield
53 Ord Street
West Perth WA 6005

Mail: PO Box 1102
         West Perth WA 6872

T: +61 8 6363 2666
E: Brenton.S.Chatfield@conocophillips.com
W: www.conocophillips.com.au

Document Status

Version	Purpose of Document	Original	Review	Review Date
DraftA	*Issued for client review*	Dr Ryan Dunn	Dr Sasha Zigic	28/2/2017
Rev 0	*Issued for client review*	Dr Ryan Dunn	Dr Sasha Zigic	28/2/2017
Rev 1	Issued to client		Dr Sasha Zigic	14/3/2017
Rev 2	Issued to client – assessment for 3 ppm free chlorine		Dr Sasha Zigic	7/4/2017

Approval for Issue

Name	Signature	Date
Dr Sasha Zigic	*S. Zigic*	7/4/2017

Contents

Tables

Figures

1.0   Introduction

1.1   Project background

ConocoPhillips Australia Exploration Proprietary (Pty) Limited (Ltd.) (ConocoPhillips), as proponent on behalf of the current and future co-venturers, is proposing to develop natural gas resources in the Timor Sea into high quality products in a safe, reliable and environmentally responsible manner. The Barossa Area Development (herein referred to as the "project") is located in Commonwealth waters within the Bonaparte Basin, offshore northern Australia, and is approximately 300 kilometres (km) north of Darwin, Northern Territory (NT).

The development concept of the gas resource includes a floating production storage and offloading (FPSO) facility and a gas export pipeline that are located in Commonwealth jurisdictional waters. The FPSO facility will be the central processing facility to stabilise, store and offload condensate, and to treat, condition and export gas. The extracted lean dry gas will be exported through a new gas export pipeline that will tie into the existing Bayu-Undan to Darwin gas export pipeline. The lean dry gas will then be liquefied for export at the existing ConocoPhillips operated Darwin Liquefied Natural Gas facility at Wickham Point, NT.

The FPSO facility includes cooling water flows as part of the process. The cooling water will be used to regulate the temperature in the system, and generally involves a once-through circuit, where ambient seawater is drawn in from deep seawater intakes, passed through the system and discharged as a thermal waste stream below the sea surface. To avoid bio-fouling of the pipe work and heat exchangers, dosing with chlorine is undertaken, leaving a residual concentration in the discharged water. In summary, cooling water is generally characterised by elevated temperatures and some residual concentrations of antifoulant, generally sodium hypochlorite.

To assess the change in temperature and the residual chlorine concentrations in the cooling water stream, ConocoPhillips commissioned RPS to undertake a dispersion modelling study. The coordinate of the indicative release location is presented in Table 1 and graphically in Figure 1. The purpose of the modelling was to assist in understanding the potential area that may be influenced by the routine discharge of cooling water based on the engineering information available in the early stage of the project design phase.

The potential area that may be influenced by the cooling water discharge stream was assessed for three distinct seasons; (i) summer (December to the following February), (ii) the transitional periods (March and September to November) and (iii) winter (April to August). This approach assists with identifying the environmental values and sensitivities that would be at risk of exposure on a seasonal basis.

The closest environmental values and sensitivities to the modelled release location are submerged shoals and banks including Lynedoch Bank (70 km to the south-east), Evans Shoal (64 km to the west) and Tassie Shoal (74 km to the south-west).

Table 1 Barossa offshore development area cooling water dispersion modelling study release location

Release location	Latitude	Longitude	Water depth (mLAT)
Barossa offshore development area release location	9° 52' 35.8" S	130° 11' 8.4" E	~230
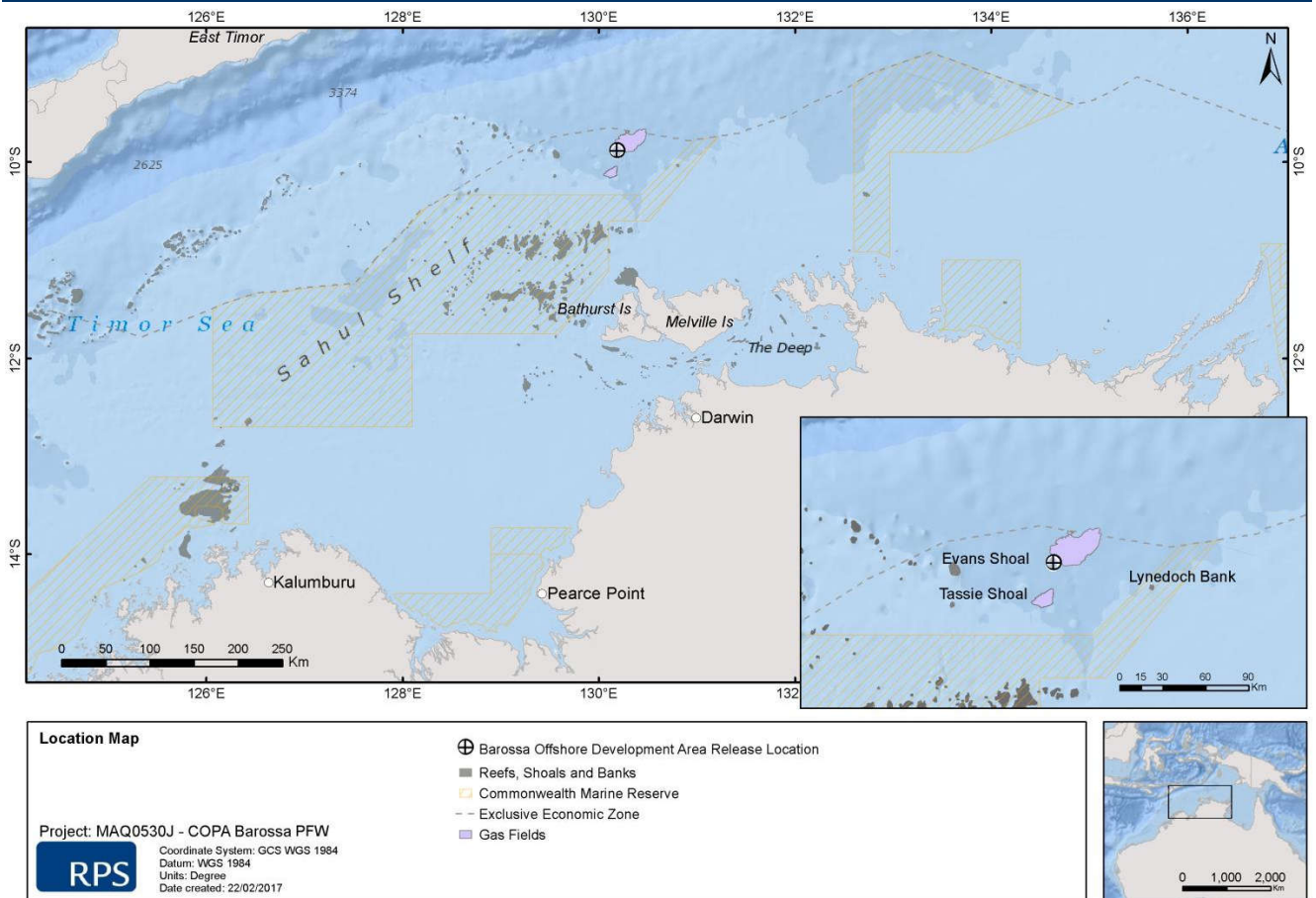
Figure 1 Map of the Barossa offshore development area cooling water modelling study release location

2.0 Dispersion modelling

The physical mixing of the cooling water stream can be separated into two distinct zones; near-field and far-field.

The near-field zone is defined by the region where the levels of mixing and dilution are controlled by the plume's initial jet momentum and the buoyancy flux, resulting from the density difference. When the plume encounters a boundary such as the water surface, seabed or density stratification layer, the near-field mixing is complete and the far-field mixing begins. During the far-field phase, the plume is transported and mixed by the ambient currents.

Therefore, to accurately determine the dilution and the mixing zone of the cooling water stream, the effect of near-field mixing needs to be considered first, followed by an investigation of the far-field mixing. Section 2.1 and Section 2.2 describe the near-field and far-field dispersion model. The physical mixing of the cooling water stream can be separated into two distinct zones; near-field and far-field.

2.1 Near-field model

2.1.1 Description

The near-field mixing of the cooling water discharge stream was predicted using the fully three-dimensional flow model, Updated Merge (UM3). The UM3 model is used for simulating single and multi-port submerged

discharges and is part of the Visual Plumes suite of models maintained by the United States Environmental Protection Agency (Frick et al. 2003).

The UM3 model has been extensively tested for various discharges and found to predict the observed dilutions more accurately (Roberts and Tian 2004) than other near-field models (e.g. RSB or CORMIX).

In this Lagrangian model, the equations for conservation of mass, momentum, and energy are solved at each time-step, giving the dilution along the plume trajectory. To determine the growth of each element, UM3 uses the shear (or Taylor) entrainment hypothesis and the projected-area-entrainment hypothesis. The flows begin as round buoyant jets issuing from one side of the diffuser and can merge to a plane buoyant jet (Carvalho et al. 2002). Model output consists of plume characteristics, including centerline dilution, rise-rate, width, centreline height and diameter of the plume. Dilution is reported as the "effective dilution", which is the ratio of the initial concentration to the concentration of the plume at a given point, following Baumgartner et al. (1994).

2.1.2   Model setup

The cooling water discharge characteristics are summarised in Table 20. The cooling water discharge was modelled 10 m below the water surface through a single outlet, and was anticipated to have a temperature of 45°C and initial chlorine concentration 3,000 parts per billion (ppb).

Additional input data used to setup the near-field model included range of current speeds, water temperature and salinity as a function of depth. Defining the water temperature and salinity is important to correctly replicate the buoyancy of the plume. The buoyancy dynamics in this case will be dominated by the temperature and salinity differences between the cooling water plume and receiving waters. Table 3 presents the measured water temperature and salinity data collected by Fugro Survey Pty Ltd (Fugro) (2015) as part of the Barossa marine studies program. The minimum water temperature at 30 m below mean sea level (BMSL) was used as it represents the most conservative conditions considering water temperature varies with depth and would be warmer at the surface in comparison to temperatures at 30 m.

Table 4 presents the 5th, 50th and 95th percentiles of current speeds, which reflect contrasting dilution and advection cases:

- 5th percentile current speed: weak currents, low dilution and slow advection
- 50th percentile (median): medium current speed, moderate dilution and advection
- 95th percentile current speed: strong currents, high dilution and rapid advection to nearby areas.

The 5th percentile, 50th percentile (median) and 95th percentile values are referenced as weak, medium and strong current speeds, respectively.

Table 2 Cooling water discharge and pipe configuration characteristics summary

Parameter	Value/design
Flow rate (m³/day)	Minimum flow rate: 288,000 Maximum flow rate: 360,576
Outlet pipe internal diameter (m)	1
Pipe orientation	Vertically downward
Depth of pipe below sea surface (m)	10
Discharge salinity (practical salinity units (PSU))	33.6–34.1 (variation based on ambient mean seasonal conditions)
Discharge water temperature (°C)	45
Initial chlorine concentration (ppb)	3,000

Table 3 Water temperature and salinity model inputs

Parameter	Season		
	Summer	Transitional	Winter
Ambient minimum water temperature (°C) (30 m BMSL)	25.4	24.7	26.3
Ambient mean salinity (Practical Salinity Units (PSU)) (30 m BMSL)	34.1	33.6	33.6

Table 4 Seasonal ambient percentile current speeds, strength and predominant direction as a function of water depth at the release location

Depth below the water surface (m)	Parameter	Reporting current strength	Season					
			Summer		Transitional		Winter	
			Speed (m/s)	Predominant direction	Speed (m/s)	Predominant direction	Speed (m/s)	Predominant direction
0	5th percentile	Weak	0.04	East	0.05	West-south-west	0.03	South-west
	50th percentile	Medium	0.11		0.14		0.11	
	95th percentile	Strong	0.27		0.29		0.27	
10	5th percentile	Weak	0.03	East	0.03	South-west	0.04	South-west
	50th percentile	Medium	0.09		0.12		0.12	
	95th percentile	Strong	0.23		0.26		0.25	
20	5th percentile	Weak	0.03	East-south-east	0.03	South-west	0.03	South-west
	50th percentile	Medium	0.08		0.11		0.12	
	95th percentile	Strong	0.20		0.24		0.24	

2.2 Far-field model

2.2.1 Description

The far-field modelling expands on the near-field model predictions as it also takes into account the time-varying nature of currents, together with the potential for recirculation of the plume back to the discharge location. In the latter case, near-field concentrations can be increased due to the discharge plume mixing with the remnant plume from an earlier time.

CHEMMAP is an advanced three-dimensional discharge and plume behaviour model that calculates the fate of discharges in the far-field (wider region). Detailed presentations of the model can be found in French McCay and Isaji (2004) and French McCay et al. (2006).

CHEMMAP predicts the trajectory and fate of a wide variety of chemical products, including floating, sinking, soluble and insoluble chemicals and product mixtures. The chemical fates model estimates the distribution of the chemical (as mass and concentrations) on the water surface, on shorelines, in the water column and in the sediments. The three-dimensional model separately tracks surface slicks, entrained droplets or particles of pure chemical, chemical adsorbed to suspended particulates, and dissolved chemical. Processes that are simulated include spreading, transport, dispersion, evaporation-volatilisation, entrainment, dissolution, partitioning, sedimentation, and degradation.

CHEMMAP is a Lagrangian model that uses a set of particles to represent the discharge. Each particle represents a portion of the discharge, by mass, and the particles are released at a given rate to represent the rate of the discharge (mass per unit time). These particles are moved in three-dimensions over each subsequent time-step according to the governing equations within each of the model stages. Particles are transported in three dimensions as defined by currents and horizontal and vertical mixing processes. Concentration of the constituent is predicted over time by counting the number of particles that fall within a given depth level within a given grid cell and converting this value to mass per unit volume.

2.3 Model setup

The MUDMAP model simulated the discharge into a time-varying current field with the initial dilution set by the near-field results described in Section 3.1.

The two cooling water flow rates were modelled as a constant discharge for each month during 2010, 2012 and 2014. Once the results were complete, they were reported on a combined seasonal basis: (i) summer (December to the following February); (ii) the transitional (March, April, September to November) and (iii) winter (May to August).

CHEMMAP uses a three-dimensional grid to represent the water depth and bathymetric profiles of the area. Due to the rapid mixing and small-scale influences of the discharge, it was necessary to use a fine grid with a resolution of 50 m x 50 m to track the movement and fate of the plume. The extent of the grid region measured approximately 80 km (longitude or x-axis) x 80 km (latitude or y-axis). Sensitivity testing for the 50 m grid cell size was performed in order to achieve similar dilution rates as calculated by the near-field modelling.

The model used sodium hypochlorite as a surrogate for the free chlorine to enable the results to be compared to guideline values. Therefore, the chemical and physical properties were directly accounted for in the model (e.g. Shams El Din et al. 2000; Zeng et al. 2009).

Table 5 presents a summary of the far-field model parameters used to simulate the cooling water discharge during the three seasons and two flow rates.

Spatially constant, conservative horizontal and vertical dispersion coefficients were used to control the exchange of the chlorien in the horizontal and vertical directions respectively. The coefficients were selected

following extensive sensitivity testing in order to recreate similar plume characteristics and dilutions at the end of the near-field mixing.

Table 5 Summary of the far-field cooling water model inputs

Parameter	Value/design
Years simulated	• 2010 (La Niña conditions) • 2012 (neutral/mixed) • 2014 (El Niño conditions)
Seasons (months simulated and reported)	• Summer (December, January, February) • Transitional periods (March, April, September to November) • Winter (May to August)
Total months modelled and analysed per flow rate	36
Flow rate (m^3/day)	Minimum flow rate: 288,000 Maximum flow rate: 360,576
Discharge type	Continuous
Period of discharge (days)	Entire month
Initial chlorine concentration (ppb)	3,000
Cooling water discharge salinity (PSU)	33.6–34.1 (variation based on ambient mean seasonal conditions)
Cooling water discharge temperature (^{o}C)	45

2.4   Interannual variability

The region is strongly affected by the strength of the Indonesian Throughflow, which fluctuates from one year to the next due to the exchange between the Pacific and Indian Oceans. Therefore, in order to examine the potential range of variability, the Southern Oscillation Index (SOI) data sourced from the Australian Bureau of Meteorology was used to identify interannual trends for the last 10 years (2005–2014). The SOI broadly defines neutral, El Niño (sustained negative values of the SOI below −8 often indicate El Niño episodes) and La Niña (sustained positive values of the SOI above +8 are typical of La Niña episodes) conditions based on differences in the surface air-pressure between Tahiti on the eastern side of the Pacific Ocean and Darwin (Australia), on the western side (Rasmusson and Wallace 1983, Philander 1990). El Niño episodes are usually accompanied by sustained warming of the central and eastern tropical Pacific Ocean and a decrease in the strength of the Pacific trade winds. La Niña episodes are usually associated with converse trends (i.e. increase in strength of the Pacific trade winds).

Figure 2 shows the SOI monthly values and Figure 3 shows the surface ocean current roses for the period 2004–2013 at the proposed release location. Each current rose diagram provides an understanding of the speed, frequency and direction of currents, over the given year:

▪ Current speed – speed is divided into segments of different colour, ranging from 0 to greater than 1 m/s. Speed intervals of 0.2 m/s are used. The length of each coloured segment is relative to the proportion of currents flowing within the corresponding speed and direction;

▪ Frequency – each of the rings on the diagram corresponds to a percentage (proportion) of time that currents were flowing in a certain direction at a given speed;

▪ Direction – each diagram shows currents flowing towards particular directions, with north at the top of the diagram.

Based on the combination of the SOI assessment and surface ocean currents, 2010 was selected as a representative La Niña year, 2012 was selected as a representative neutral year, and 2014 was selected as an El Niño year.
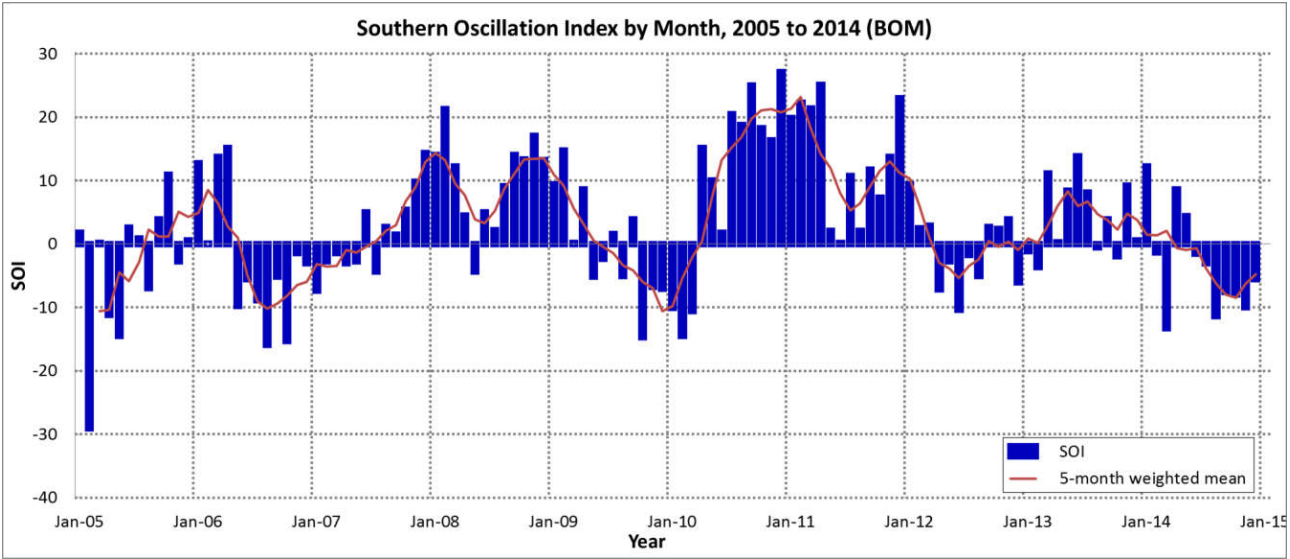
Figure 2 Monthly values of the SOI 2005-2014. Sustained positive values indicate La Niña conditions, while sustained negative values indicate El Niño conditions (Data sourced from Australian Bureau of Meteorology 2015).
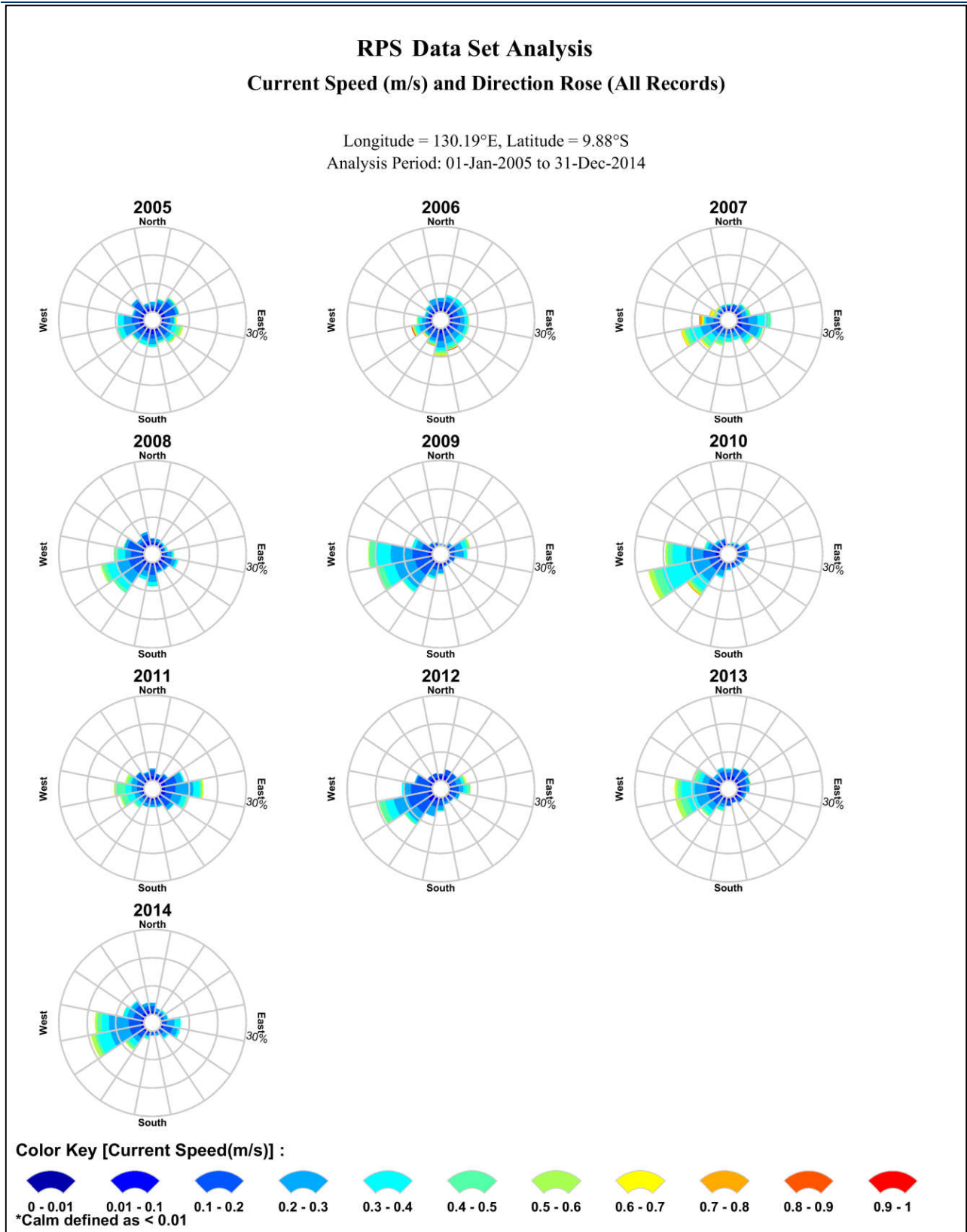
Figure 3 Annual surface ocean current rose plots within the Barossa Offshore Development Area. Derived from analysis of HYCOM ocean data for the years 2005–2014. The colour key shows the current speed (m/s), the compass shows the direction and the length of the wedge gives the percentage of the record for a particular speed and direction combination.

2.5   Development of regional current data

The project is located within the influence of the Indonesian Throughflow, a large scale current system characterised as a series of migrating gyres and connecting jets that are steered by the continental shelf. This results in sporadic deep ocean events causing surface currents to exceed 1.5 m/s (approximately 3 knots).

While the ocean currents generally flow toward the southwest, year-round, the internal gyres generate local currents in any direction. As these gyres migrate through the area, large spatial variations in the speed and direction of currents will occur at a given location over time.

The influence of tidal currents is generally weaker in the deeper waters and greatest surrounding regional reefs and islands. Therefore, it was critical to include the influence of both types of currents (ocean and tides) to rigorously understand the likely discharge characteristics in the project's area of influence.

A detailed description of the tidal and ocean current data inputted into the model is provided below.

2.5.1   Tidal currents

The tidal circulation was generated using RPS's advanced ocean/coastal model, HYDROMAP. The HYDROMAP model has been thoroughly tested and verified through field measurements throughout the world over the past 26 years (Isaji and Spaulding 1984; Isaji et al. 2001; Zigic et al. 2003). In addition, HYDROMAP tidal current data has been used as input to forecast (in the future) and hindcast (in the past) condensate spills in Australian waters and forms part of the Australian National Oil Spill Emergency Response System operated by the Australian Maritime Safety Authority (AMSA).

HYDROMAP employs a sophisticated sub-gridding strategy, which supports up to six levels of spatial resolution, halving the grid cell size as each level of resolution is employed. The sub-gridding allows for higher resolution of currents within areas of greater bathymetric and coastline complexity, and/or of particular interest to a study.

The numerical solution methodology follows that of Davies (1977a, 1977b) with further developments for model efficiency by Owen (1980) and Gordon (1982). A more detailed presentation of the model can be found in Isaji and Spaulding (1984), Isaji et al. (2001) and Owen (1980).

1.1.1.1   Tidal grid setup

The HYDROMAP tidal grid was established over a domain that extended approximately 2,400 km (east–west) by 1,575 km (north–south) (Figure 4). Computational cells were square, with sizes varying from 8 km in the open waters down to 1 km in some areas, to more accurately resolve flows along the coastline, around islands and reefs, and over more complex bathymetry (Figure 5).

Bathymetry used in the model was obtained from multiple sources (Figure 6). This included bathymetry data sourced from the Geoscience Australia database and commercially available digitised navigation charts.
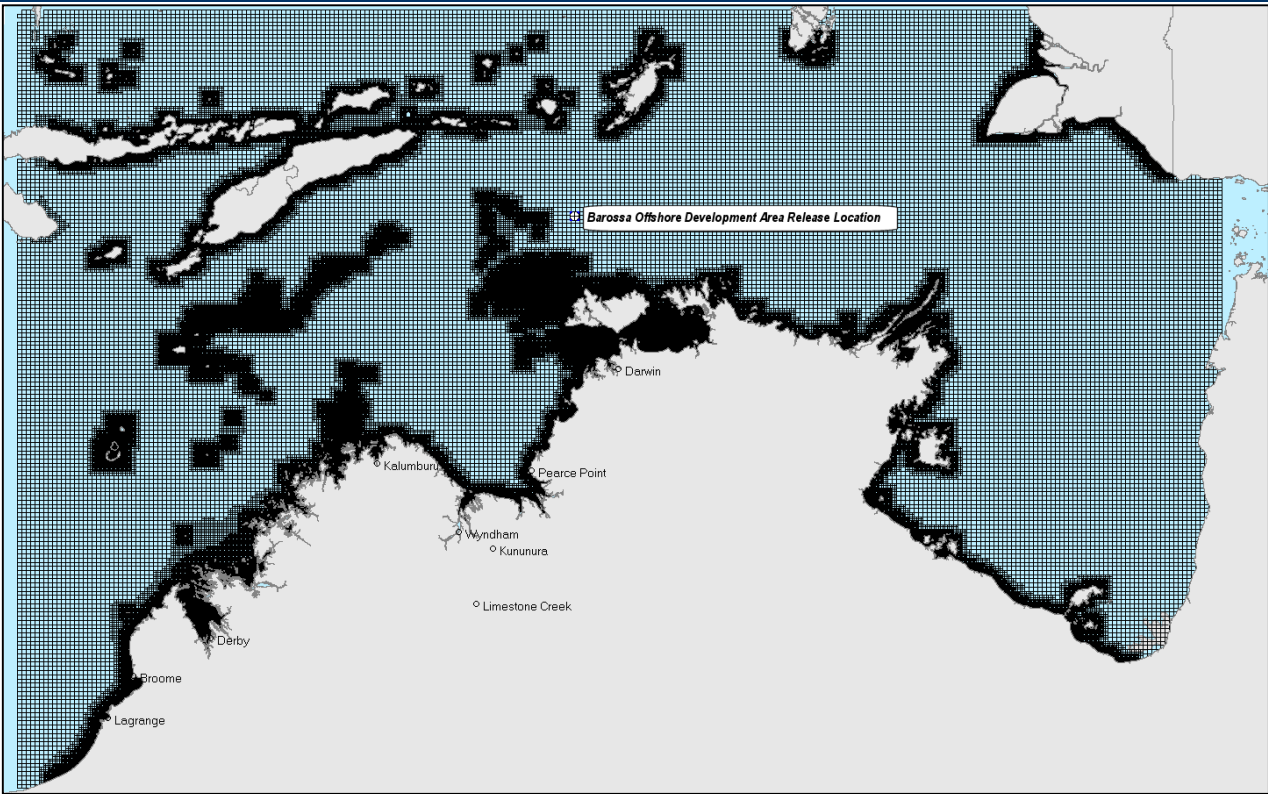
Figure 4 Map showing the extent of the tidal model grid. Note, darker regions indicate higher grid resolution.
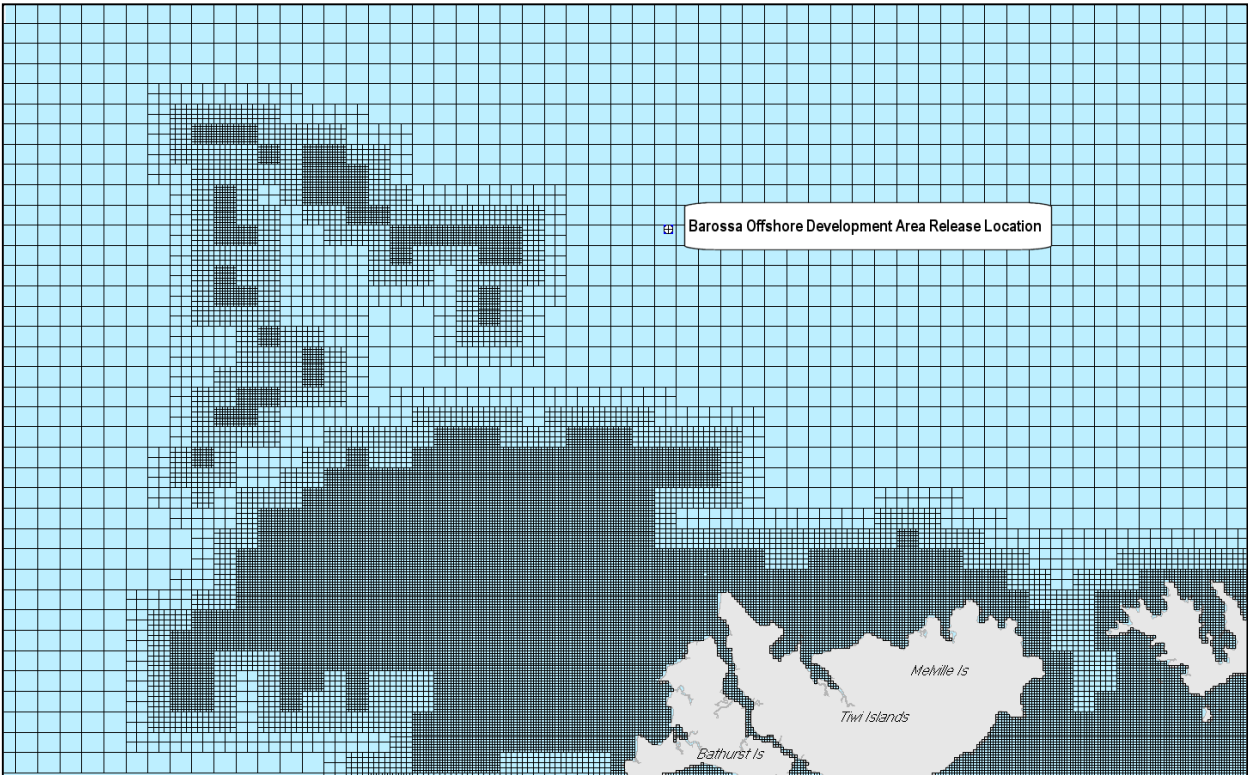
Figure 5 Zoomed in map showing the tidal model grid), illustrating the resolution sub-gridding in complex areas (e.g. islands, banks, shoals or reefs)
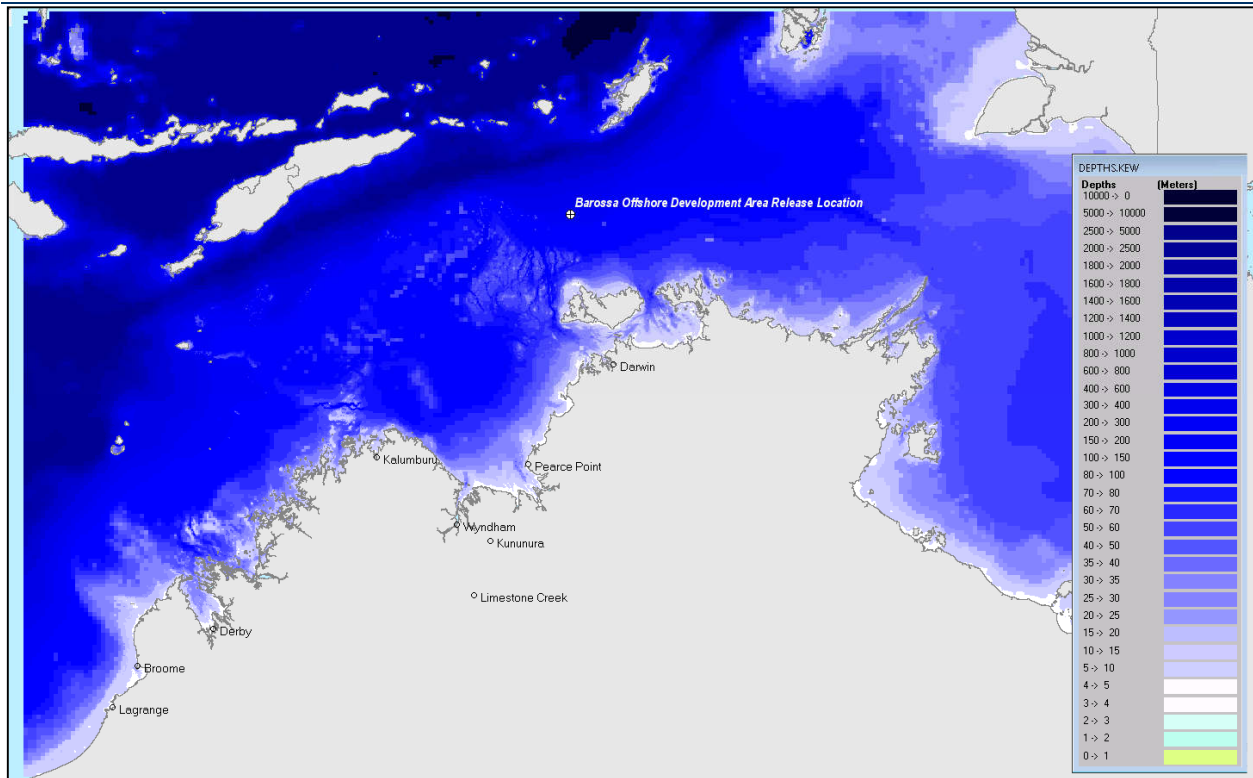
Figure 6 Map showing the bathymetry of the tidal model grid

1.1.1.2   Tidal data

The ocean boundary data for the regional model was obtained from satellite measured altimetry data (TOPEX/Poseidon 7.2) which provided estimates of the eight dominant tidal constituents at a horizontal scale of approximately 0.25 degrees. Using the tidal data, surface heights were firstly calculated along the open boundaries, at each time step in the model.

The Topex-Poseidon satellite data is produced and quality controlled by the National Aeronautics and Space Administration (NASA). The satellites, equipped with two highly accurate altimeters that are capable of taking sea level measurements to an accuracy of less than 5 cm, measured oceanic surface elevations (and the resultant tides) for over 13 years (1992–2005; see Fu et al., 1994; NASA/Jet Propulsion Laboratory 2013a; 2013b). In total these satellites carried out 62,000 orbits of the planet. The Topex-Poseidon tidal data has been widely used amongst the oceanographic community, being the subject of more than 2,100 research publications (e.g. Andersen 1995, Ludicone et al. 1998, Matsumoto et al. 2000, Kostianoy et al. 2003, Yaremchuk and Tangdong 2004, Qiu and Chen 2010). As such the Topex/Poseidon tidal data is considered accurate for this study.

2.5.2   Ocean currents

Data describing the flow of ocean currents was obtained from the Hybrid Coordinate Ocean Model (HYCOM) (see Chassignet et al. 2007, 2009), which is operated by the HYCOM Consortium, sponsored by the Global Ocean Data Assimilation Experiment (GODAE). HYCOM is a data-assimilative, three-dimensional ocean model that is run as a hindcast, assimilating time-varying observations of sea surface height, sea surface temperature and in-situ temperature and salinity measurements (Chassignet et al. 2009). The HYCOM predictions for drift currents are produced at a horizontal spatial resolution of approximately 8.25 km (1/12th of a degree) over the region, at a frequency of once per day. HYCOM uses isopycnal layers in the open, stratified ocean, but uses the

layered continuity equation to make a dynamically smooth transition to a terrain following coordinate in shallow coastal regions, and to z-level coordinates in the mixed layer and/or unstratified seas.

For this modelling study, the HYCOM hindcast currents were obtained for the years 2010 to 2014 (inclusive). Figure 7 shows the seasonal surface current roses distributions adjacent to the release location by combining 2010, 2012 and 2014. The data shows that the surface current speeds and directions varied between seasons. In general, during transitional conditions (March, April and September to November) currents were shown to have the strongest average speed (average speed of 0.15 m/s with a maximum of 0.39 m/s) and tended to flow to the west-southwest. During summer (December to February) and winter (May to August) conditions the current flow was more variable though mostly toward the east and west, respectively. The average and maximum speeds during summer was 0.11 m/s and 0.41 m/s, respectively. During winter the average was 0.13 m/s and 0.47 m/s as the maximum.
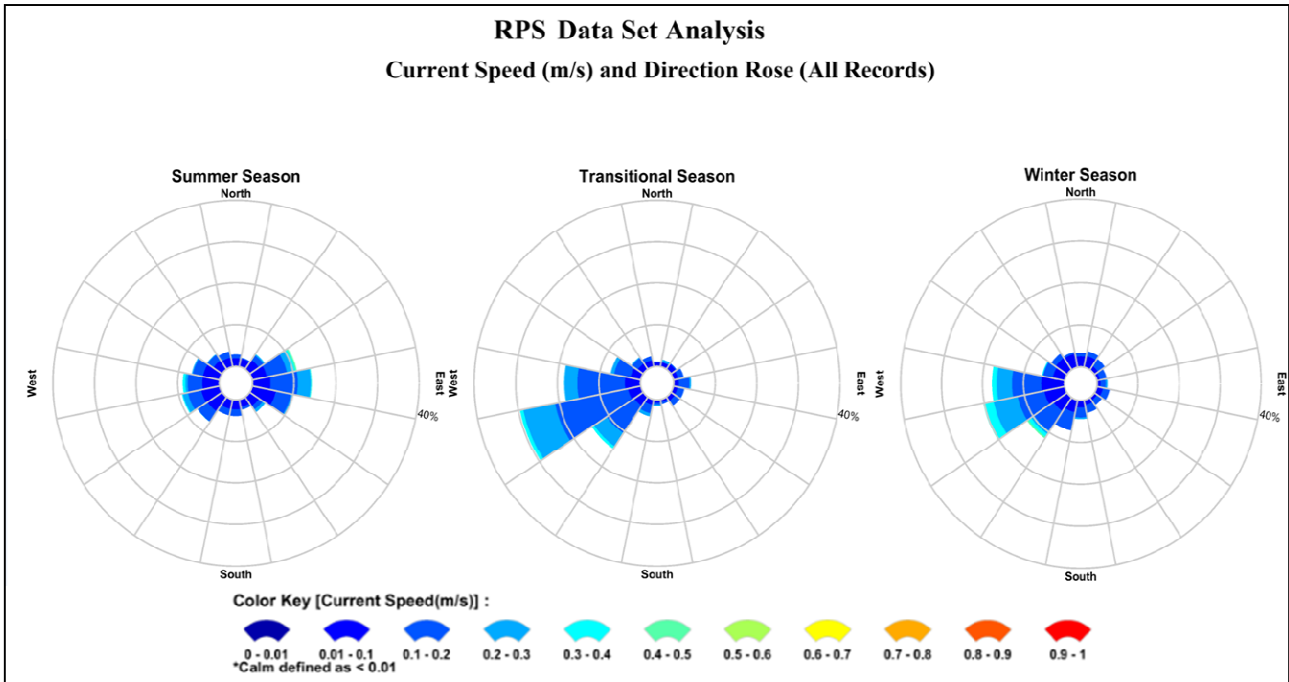
Figure 7 Seasonal surface current rose plots adjacent to the release location. Data was derived from the HYCOM ocean currents for years, 2010, 2012 and 2014. The colour key shows the current magnitude (m/s), the compass direction provides the current direction flowing TOWARDS and the length of the wedge gives the percentage of the record for a particular speed and direction combination.

Figure 8 shows example screenshots of the predicted HYCOM ocean currents during summer and winter conditions. The colours of the arrows indicate current speed (m/s).

In addition, Figure 9 to Figure 11 show the monthly surface current rose plots adjacent to the release location for 2010, 2012 and 2014, respectively. The data is derived by combining the ocean currents and tidal currents.
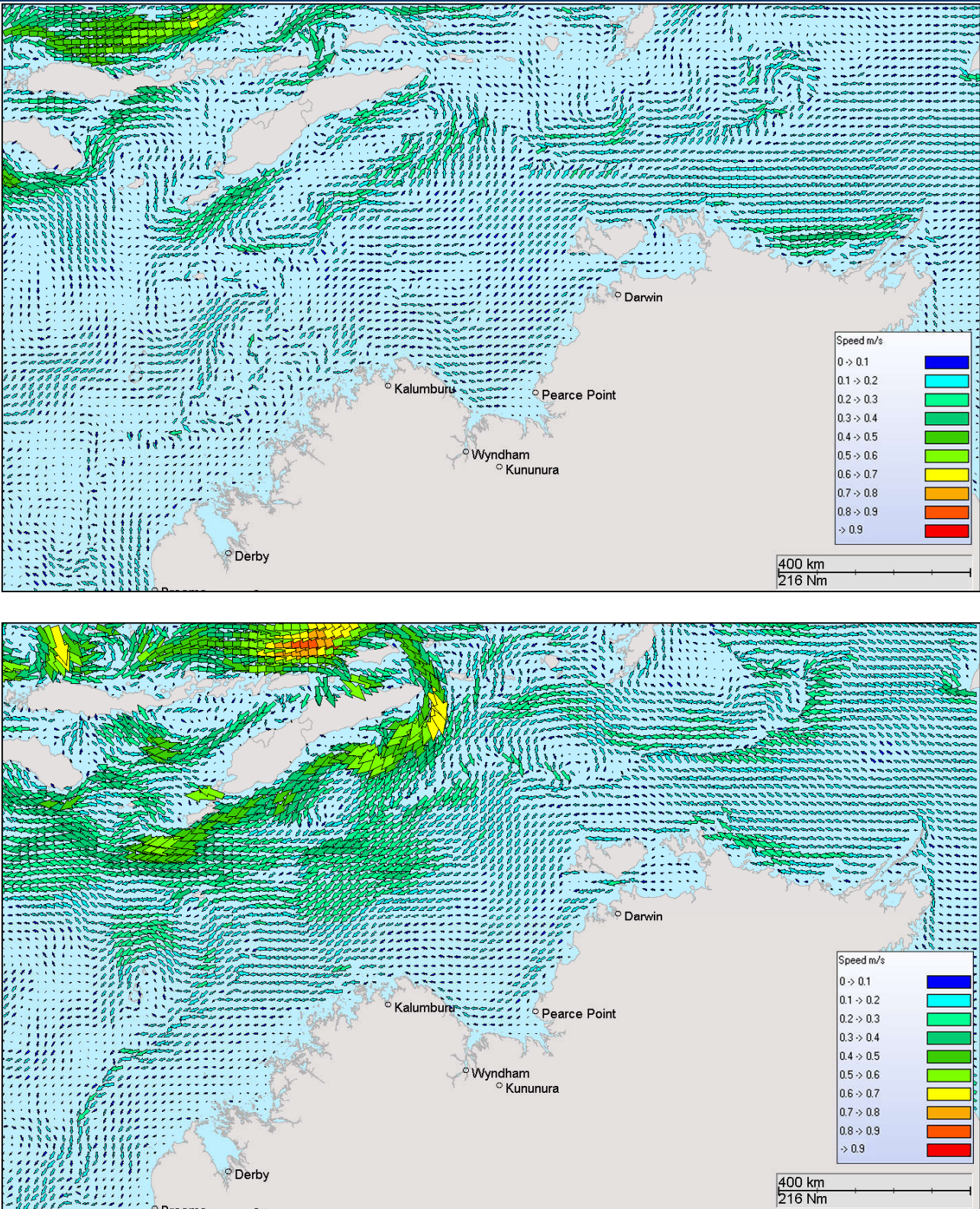
Figure 8 Modelled HYCOM surface ocean currents on the 6th February 2012, summer conditions (upper image) and 11th May 2012, winter conditions (lower image). Derived from the HYCOM ocean hindcast model (Note: for image clarity only every 2nd vector is displayed).
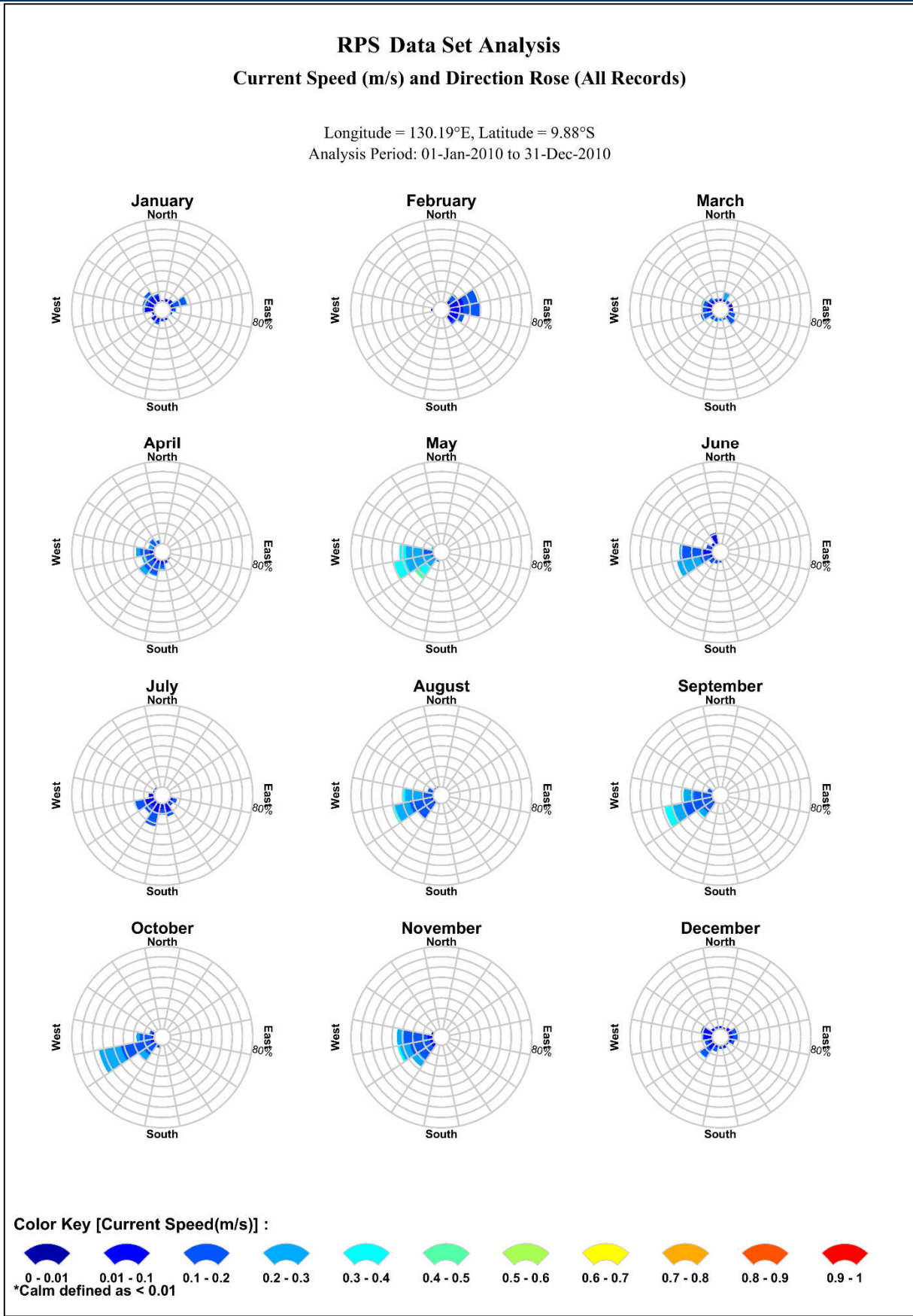
Figure 9 Monthly surface current rose plots adjacent to the model release location. Derived from analysis of HYCOM ocean data and tidal data for 2010 (La Niña year). The colour key shows the current speed (m/s), the compass shows the direction and the length of the wedge gives the percentage of the record for a particular speed and direction combination.

RPS Data Set Analysis

Current Speed (m/s) and Direction Rose (All Records)

Longitude = 130.19°E, Latitude = 9.88°S
Analysis Period: 01-Jan-2012 to 31-Dec-2012

Color Key [Current Speed(m/s)] :

0 - 0.01 0.01 - 0.1 0.1 - 0.2 0.2 - 0.3 0.3 - 0.4 0.4 - 0.5 0.5 - 0.6 0.6 - 0.7 0.7 - 0.8 0.8 - 0.9 0.9 - 1
*Calm defined as < 0.01
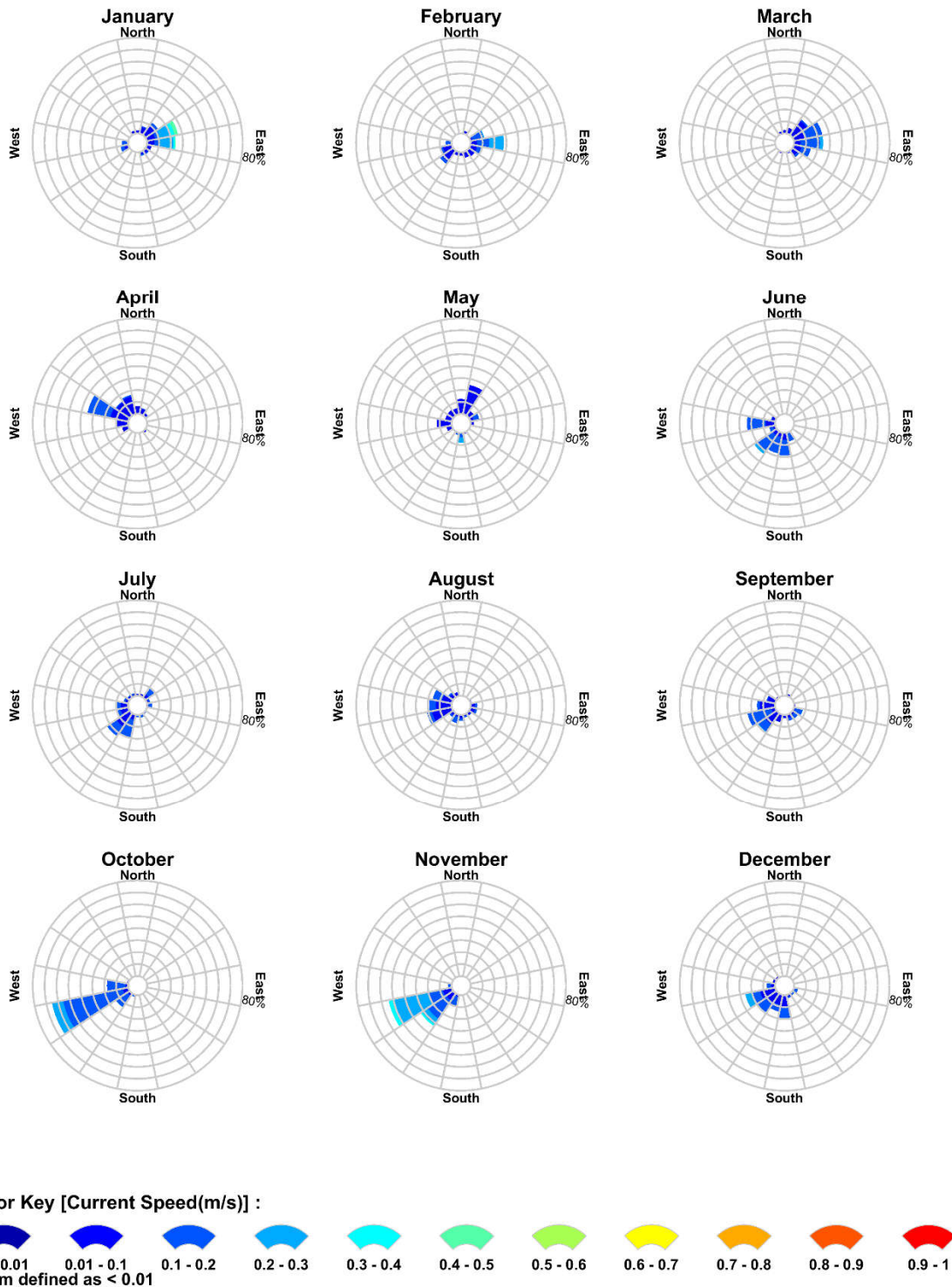
Figure 10 Monthly surface current rose plots adjacent to the model release location. Derived from analysis of HYCOM ocean data and tidal data for 2012 (neutral year). The colour key shows the current speed (m/s), the compass shows the direction and the length of the wedge gives the percentage of the record for a particular speed and direction combination.
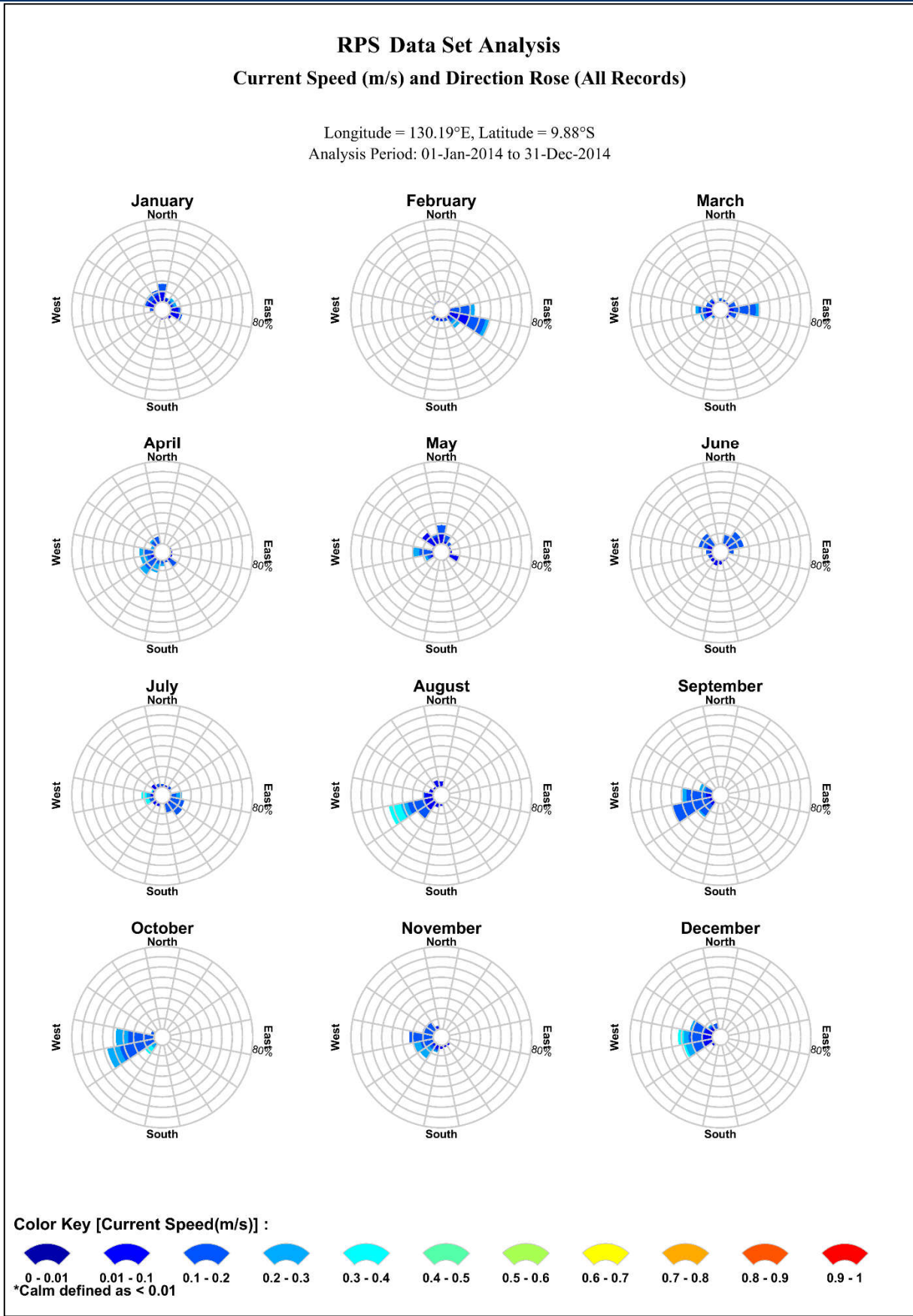
Figure 11 Monthly surface current rose plots adjacent to the model release location. Derived from analysis of HYCOM ocean data and tidal data for 2014 (El Niño year). The colour key shows the current speed (m/s), the compass shows the direction and the length of the wedge gives the percentage of the record for a particular speed and direction combination.

2.5.3 Tidal and current model validation

Fugro measured water levels and currents (speed and directions) at three locations within the Barossa offshore development area as part of the Barossa marine studies program (Figure 12, Fugro 2015). The measured data from the survey was made available to validate the predicted currents, which corresponds to the three identified seasons of the region (i.e. summer (December to February), transitional (March and September to November) and winter (April to August)).
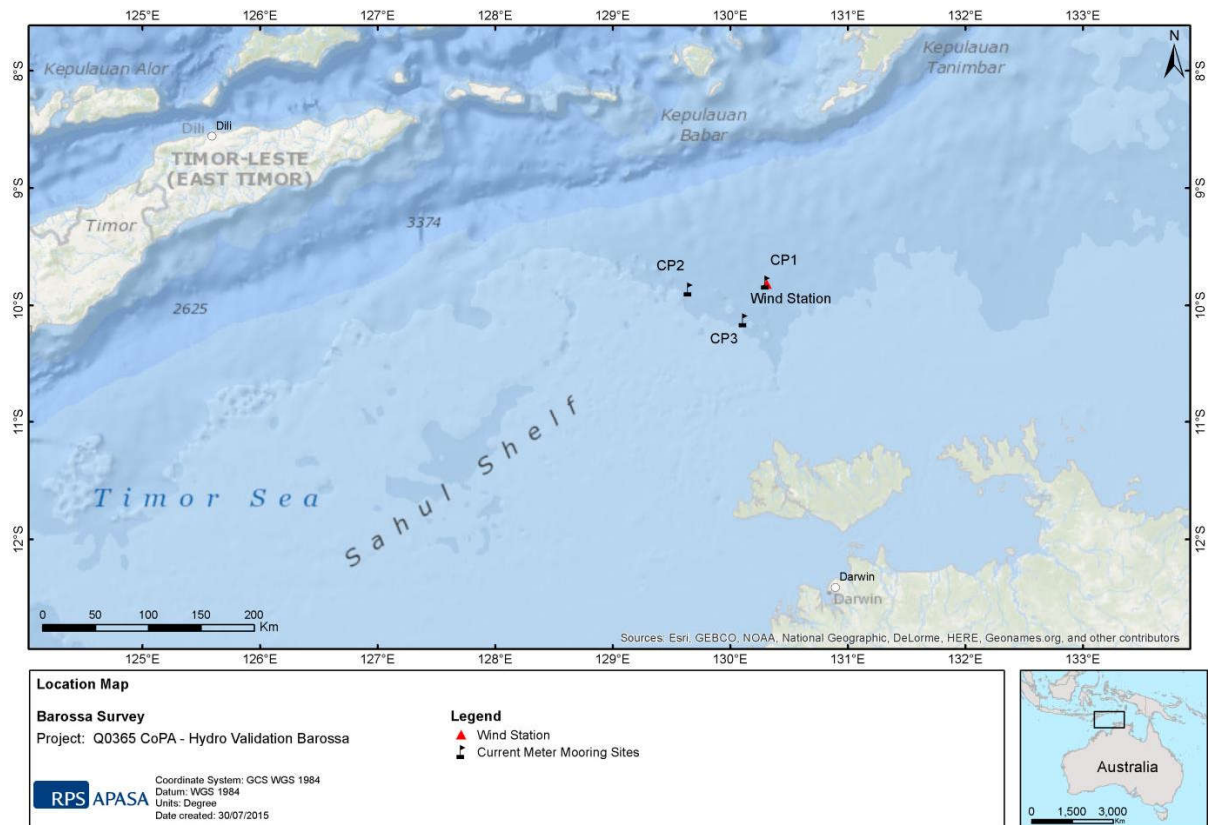
Figure 12 Locations of the CP1, CP2 and CP3 current meter moorings and the wind station

As an example, Figure 13 shows a comparison between the measured and predicted water levels at CP1 from 28 October 2014 to 14 March 2015. The figure shows a strong agreement in tidal amplitude and phasing throughout the entire deployment duration at the CP1 location.

To provide a statistical quantification of the model accuracy, comparisons were performed by determining the deviations between the predicted and measured data. As such, the root-mean square error (RMSE), root-mean square percentage (RMS %) and relative mean absolute error (RMAE) were calculated. Qualification of the RMAE ranges are reported in accordance with Walstra et al. (2001).

Table 6 shows the model performance when compared with measured water levels at CP1 from 28 October to 14 March 2015. According to the statistical measure, the HYDROMAP tidal model predictions were in very good agreement with the measured water levels at CP1.
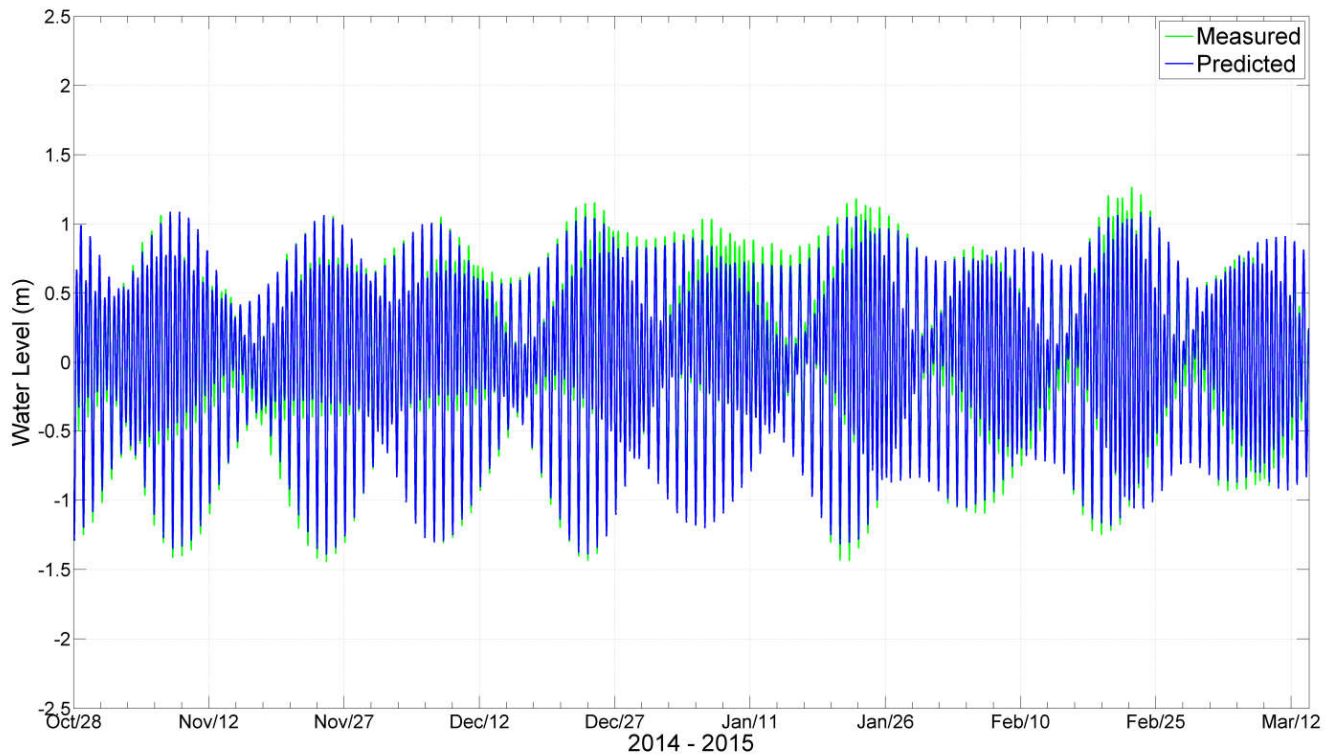
Figure 13 Comparison of measured and modelled water levels at CP1

Table 6 Statistical evaluation between measured water levels and HYDROMAP predicted water levels at CP1

Site	RMSE (m)	RMS (%)	RMAE	RMAE qualification
Mooring CP1	0.061	0.03	0.05	Very good

In addition, the HYCOM ocean currents combined with HYDROMAP tidal currents were compared to the measured current speed and directions from the CP1, CP2 and CP3 moorings. Figure 14 to Figure 16 show current comparison plots of the measured and predicted currents at each location for a range of depths (10 m, 50 m and 125 m BMSL) to highlight the differences between the wind-influenced surface layers and the mid water column.
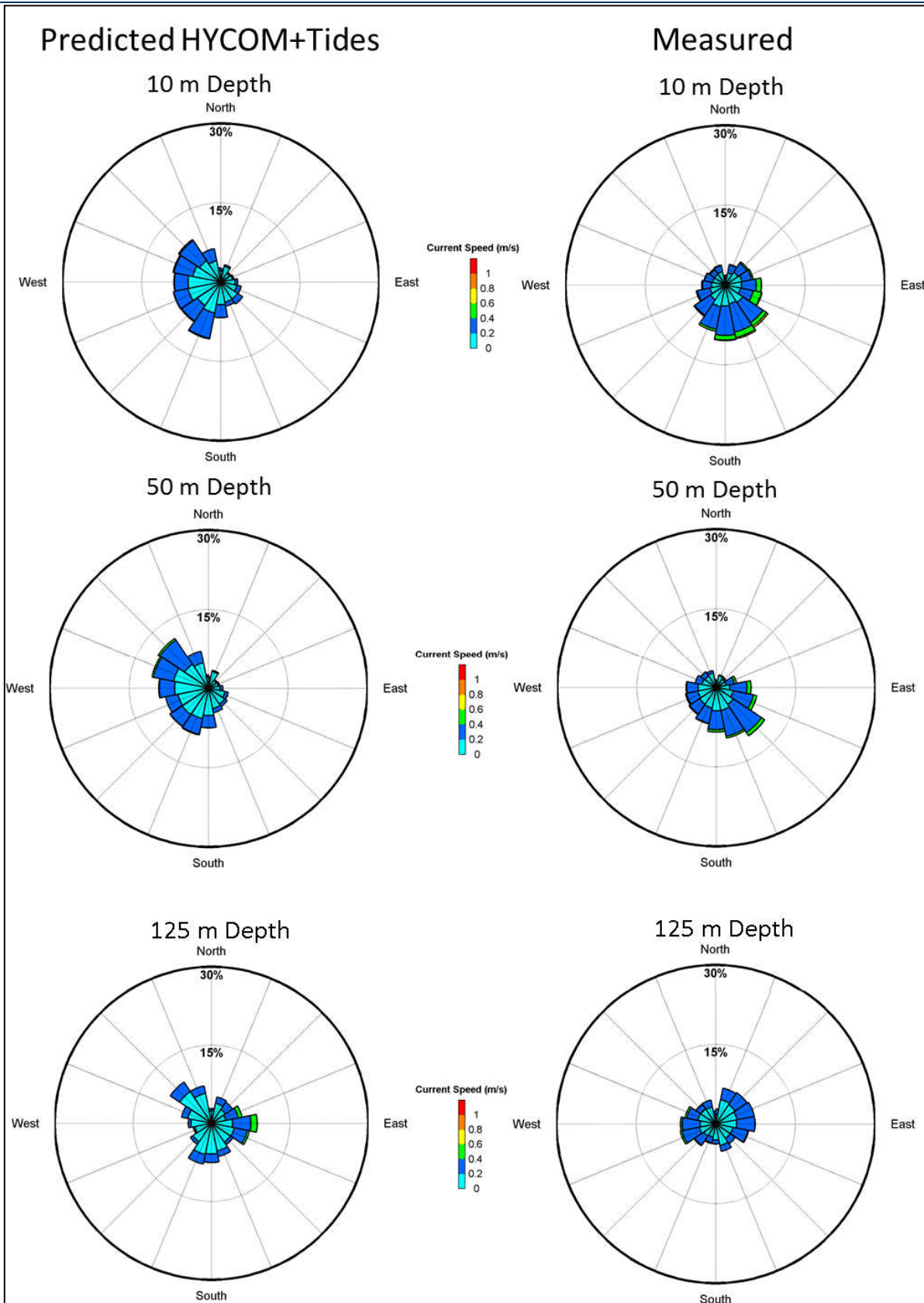
Figure 14 Comparison of predicted and measured current roses at CP1 from 9th July 2014 to 21st March 2015
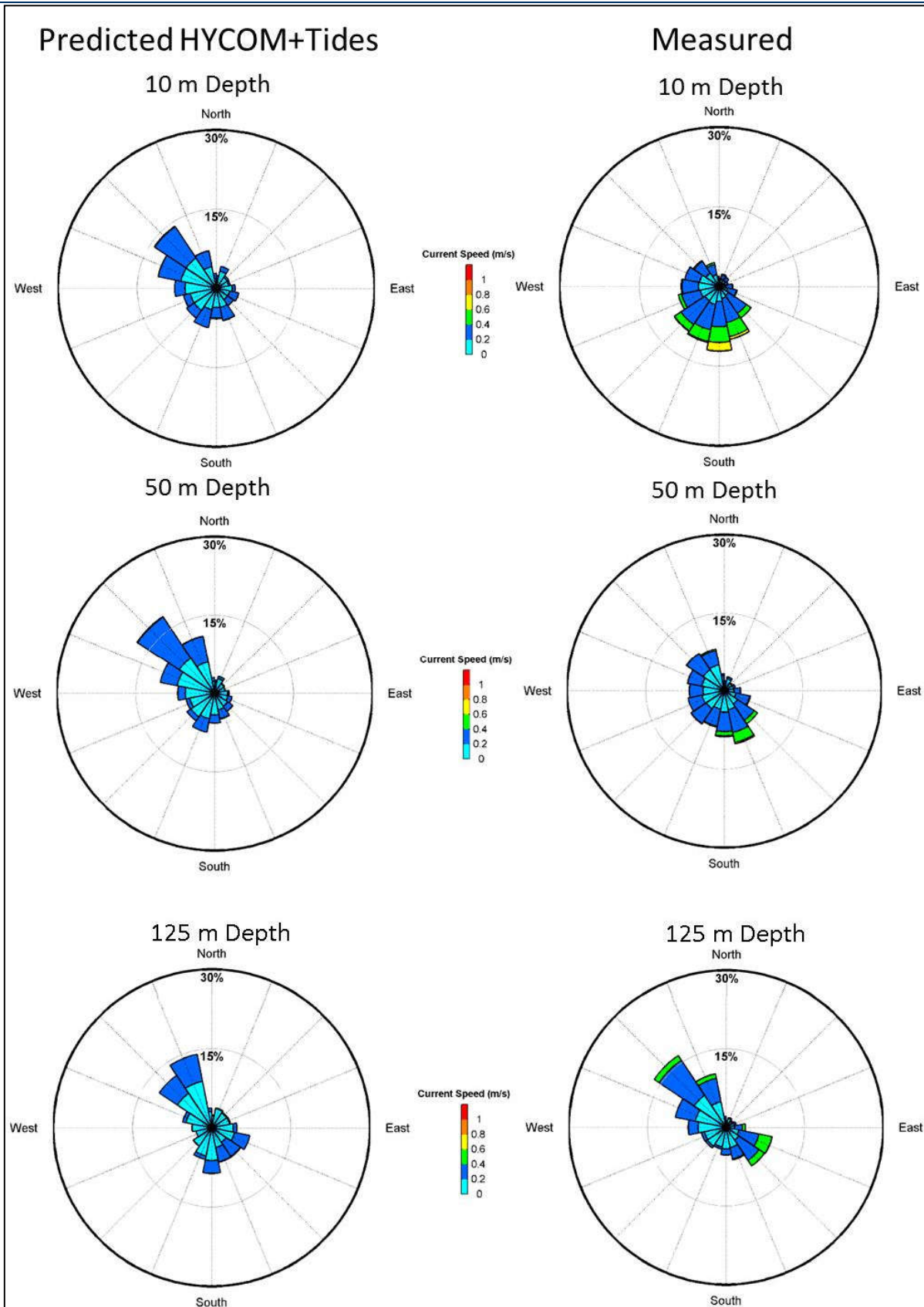
Figure 15 Comparison of predicted and measured current roses at CP2 from 10th July 2014 to 21st March 2015
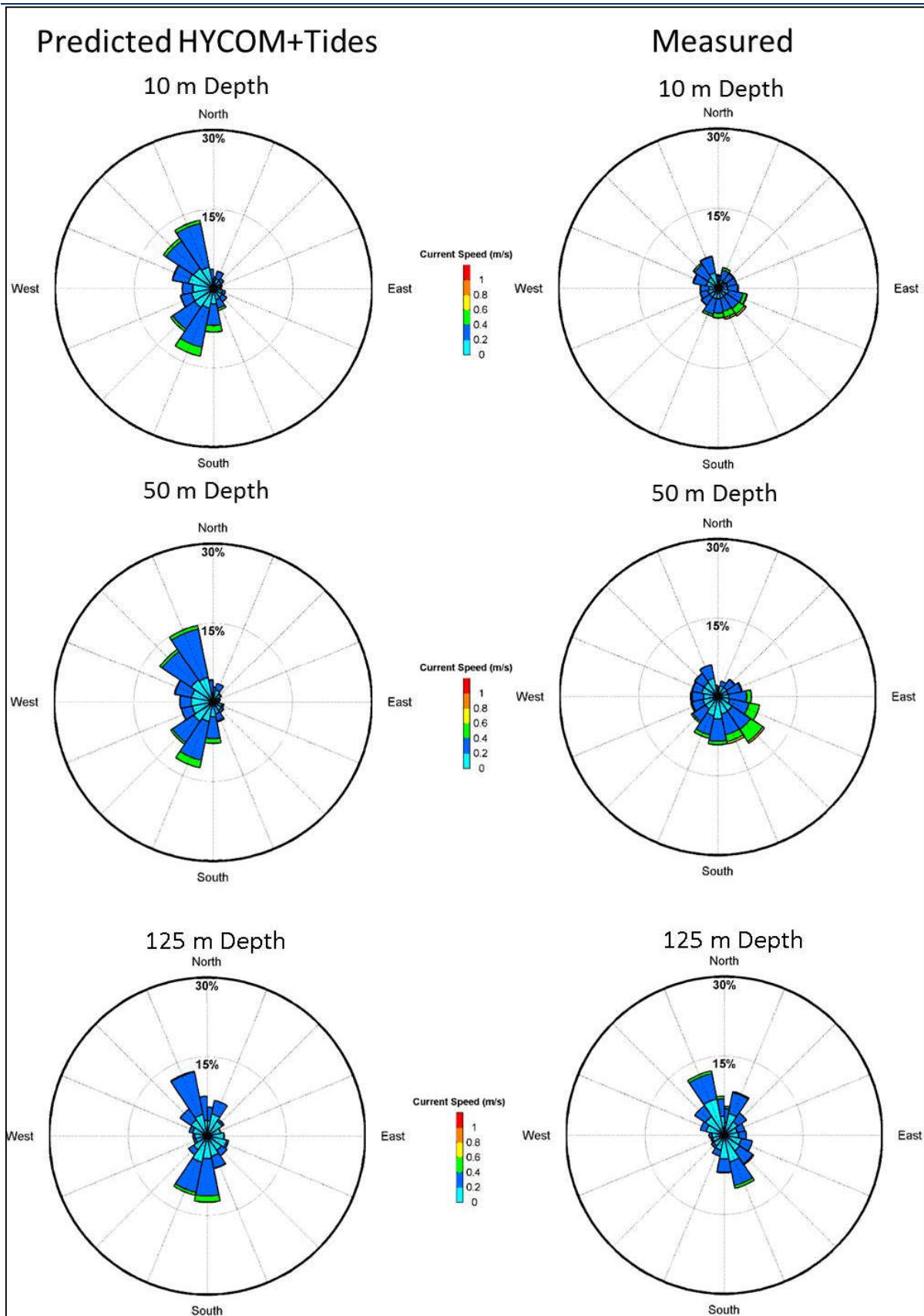
Figure 16 Comparison of predicted and measured current roses at CP3 from 9th July 2014 to 21st March 2015.

Overall, there was a good agreement between the predicted and measured currents at each site and depth. The model predictions were also able to recreate the two-layer flow which can be seen in the measured data and the reduction in current speeds as function of depth. From 10 m down to approximately 100 m below mean sea

level (BMSL) the currents generally flowed south-east, with little variation due to tidal changes. The model predictions replicated this behaviour. Below 100 m, the influence of the tides became more pronounced, rotating between a south-eastward flow and a north-westward flow with the turning of the tide. Both tidal-scale and large-scale fluctuations in currents were typically reproduced at a similar magnitude and timing.

There was some divergence between the predicted and measured currents, mostly between data from July to October inclusive, due to the occurrence of solitons (or high frequency internal waves that can produce unusually high currents) which was highlighted by Fugro (2015). Despite these variations, the statistical comparisons between the measured and predicted current speeds indicate a reasonable to very good agreement (Table 7). Therefore, it can be concluded it is a good comparison and that the predicted current data reliably reproduced the complex conditions within the Barossa offshore development area and surrounding region. The RPS APASA (2015) model validation report provides a more detail regarding the tide and current comparison.

In summary, the Fugro (2015) data provides information specifically for the Barossa offshore development area and is considered the best available and most accurate data for this particular region. This data has been provided and reviewed by RPS to confirm predicted currents applied are accurate. As a result, the current data used herein is considered best available and highly representative of the characteristics influencing the marine environment in the Barossa offshore development area.

Table 7 Statistical evaluation between averaged measured currents and HYCOM ocean current and HYDROMAP tidal current at CP1, CP2 and CP3 at varying water depths (July 2014 to March 2015)

Site	Depth (m BMSL)	RMSE (m/s)	Measured peak value (m/s)	RMSE (%)	RMAE qualification
Mooring CP1	10	0.14	0.71	20	Good
	50	0.14	0.63	22	Very good
	125	0.13	0.61	22	Very good
Mooring CP2	10	0.16	0.82	19	Reasonable
	50	0.14	0.81	17	Good
	125	0.16	0.72	22	Reasonable
Mooring CP3	10	0.15	0.88	18	Very good
	50	0.14	0.78	18	Very good
	125	0.13	0.60	21	Very good

2.6 Environmental reporting criteria

The following environmental criteria were used for the modelling study.

Temperature

The criterion of assessing that temperature is within 3˚C within 100 m from the release location was applied for the cooling water dispersion modelling study. This criterion is defined in the International Finance Corporation (IFC) Industry Environmental, Health and Safety Guideline for Offshore Oil and Gas Development (IFC 2015) and represents a commonly adopted industry standard.

Maximum extent of the chlorine

The Commonwealth Scientific and Industrial Research Organisation (CSIRO) scientific literature review on the toxicity of chlorine, for the Browse Floating LNG Development referral (Woodside Energy Ltd 2011), had found that 13 ppb corresponds to the predicted no effect concentration for acute exposure. Whereas 2 ppb as the predicted no effect concentration in the event of chronic exposure to chlorine at the 99% species protection level (Chariton and Stauber 2008). The literature review had made note that the vast majority of species will have higher tolerance compared to the 2 ppb threshold, and that only be the most sensitive species have a toxic response.

Therefore, the far-field modelling results are presented as contour maps which include concentrations of 2, 3, 4, 8, 13 and 20 ppb and corresponding dilution intervals of: 1:1,500, 1:1,000; 1:750, 1:375, 1:231, and 1:150 on the keys. The dilution intervals are based on an initial chlorine concentration of 3,000 ppb.

3.0   Modelling results

3.1   Near-field modelling

Figure 17 to Figure 22 (note the differing x- and y-axis aspect ratios) show the predicted change in temperature and dilution, under the varying flow rates (minimum and maximum), as a function of horizontal distance before reaching the sea surface, for each current speed (weak, medium and strong) and season (summer, transitional and winter). The results can also be found summarised in tabulated form in Table 8 and Table 9.

The results showed that due to plume momentum, the cooling water plume initially plunges downward creating a turbulent mixing zone ranging between approximately 40 m to 63 m for the minimum flow rate (288,000 m^3/d) and approximately 48 m to 70 m for the maximum flow rate (360,576 m^3/d) below the water surface. The cooling water plunged deeper under weak current conditions for both minimum and maximum flow rates. Once the plume lost its momentum it began to rise to the surface due to the temperature difference with ambient waters. As the plume rose through the water column, it continued to mix with ambient waters, though at a slower rate. During both flow rates, the plume was sufficiently buoyant to rise to the sea surface during all current speeds at distances less than 100 m from the release location.

Upon encountering the sea surface (i.e. end of near-field mixing), the diameter of the cooling water plume at the sea surface ranged from approximately 18 m to 37 m for the minimum flow rate and approximately 22 m to 43 m for the maximum flow rate (Table 8 and Table 9).

In all cases, the temperature of the cooling water plume was predicted to be within 3°C of the ambient (background) temperature within 100 m from the release location. **Appendix A** and **Appendix B** provide graphs of the predicted difference in temperature between the cooling water plume and ambient temperature versus distance from release location for the minimum and maximum flow rates, respectively. The temperature of the cooling water plume generally returned to within 3°C of ambient water temperature within approximately 5 m to 6 m of the discharge location, with the greatest distance of 12 m recorded in medium currents during the transitional season (minimum flow rate).

For all seasons and flow rates modelled, the primary factor influencing the dilution of the discharged cooling water plume was the speed of the current. Weak currents had little effect on the plume during the rise process and therefore it reached the surface quickly (i.e. within 5 m from the release location for the minimum flow rate and approximately 8 m for the maximum flow rate) and slowing the rate of dilution. The medium and strong currents were capable of pushing the buoyant plume horizontally up to a maximum distance of approximately 37 m and 67 m for the minimum flow rate (see Table 8), respectively, and approximately 45 m and 81 m during the maximum flow rate (see Table 9), respectively, allowing for additional mixing prior to reaching the surface. Average dilutions of the cooling water plume upon reaching the sea surface for the minimum and maximum flow rates ranged between 1:24 to 1:69 and 1:30 to 1:80, respectively.

Additionally, the minimum dilutions of the cooling water plume (i.e. dilution of plume centreline) upon the plume boundary encountering the sea surface under medium and strong constant currents were predicted to range between be 1:13 to 1:31 during the minimum flow rate and 1:15 to 1:43 during the maximum flow rate, respectively.

Note that these predictions rely on the persistence of current speed and direction over time and does not account for the build-up of the plume.
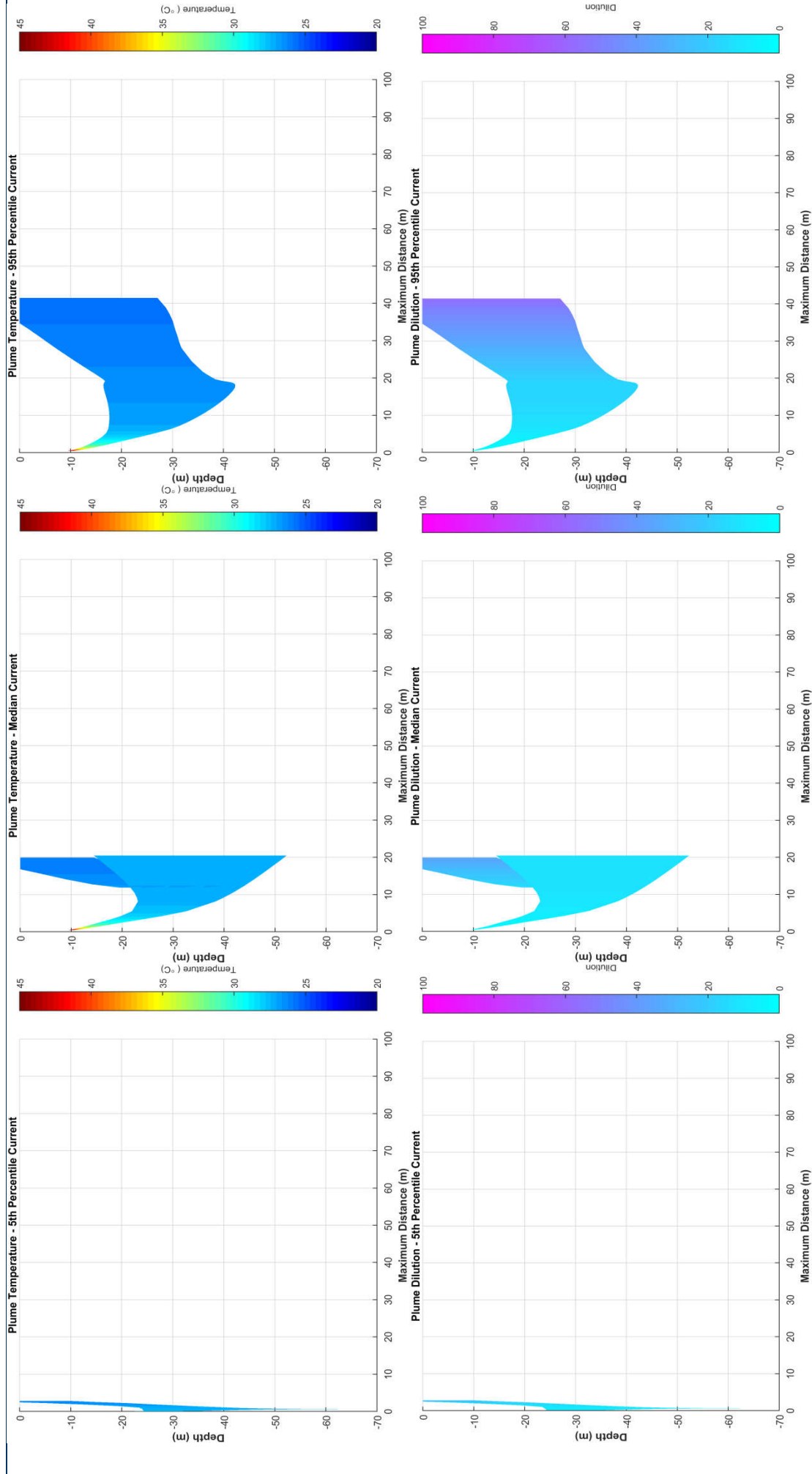
Figure 17 Near-field average temperature and dilution results for constant weak, medium and strong summer currents for the minimum flow rate (288,000 m³/d)
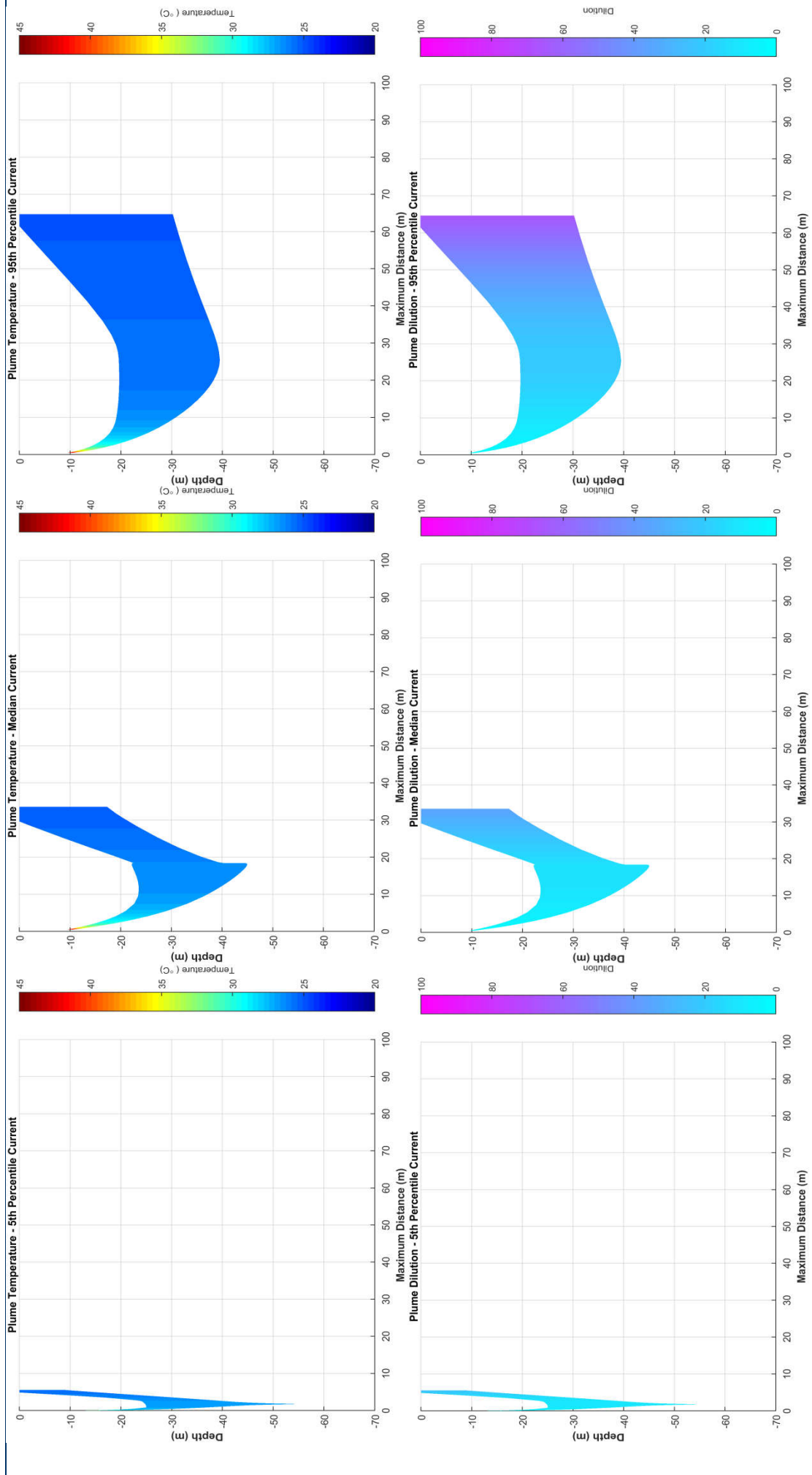
Figure 18 Near-field average temperature and dilution results for constant weak, medium and strong transitional currents for the minimum flow rate (288,000 m³/d)
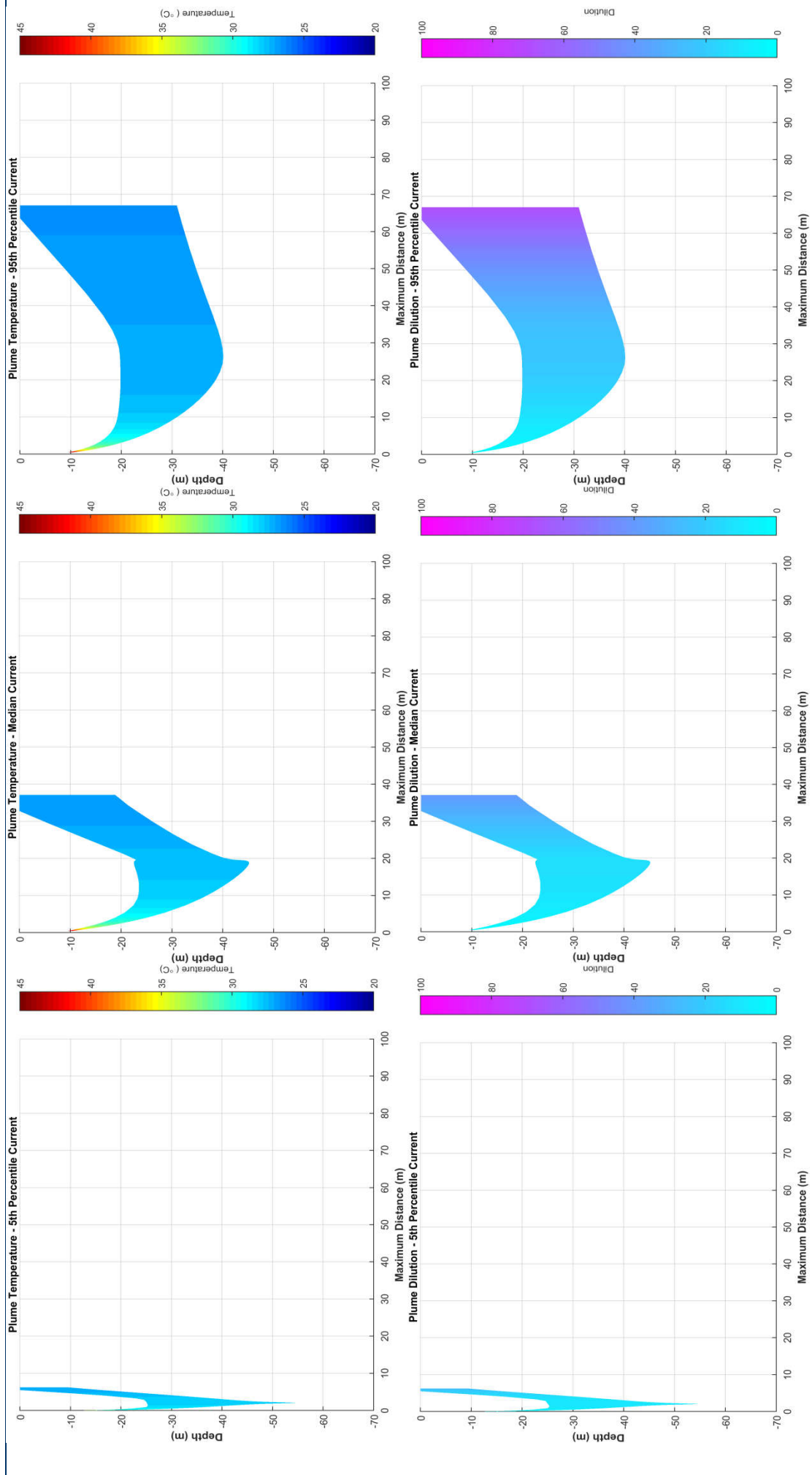
Figure 19 Near-field average temperature and dilution results for constant weak, medium and strong winter currents for the minimum flow rate (288,000 m³/d)
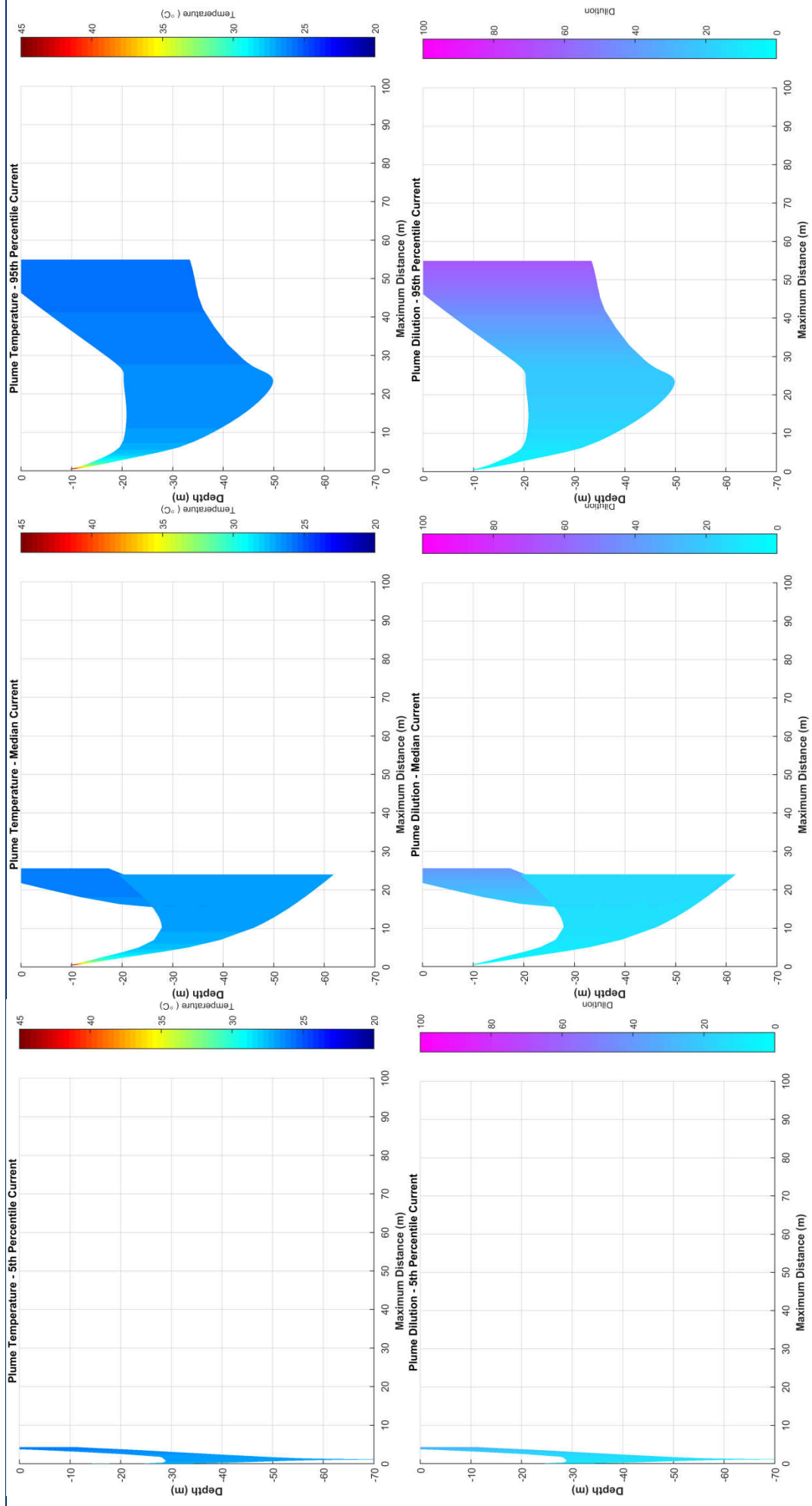
Figure 20 Near-field average temperature and dilution results for constant weak, medium and strong summer currents for the maximum flow rate (360,576 m³/d)
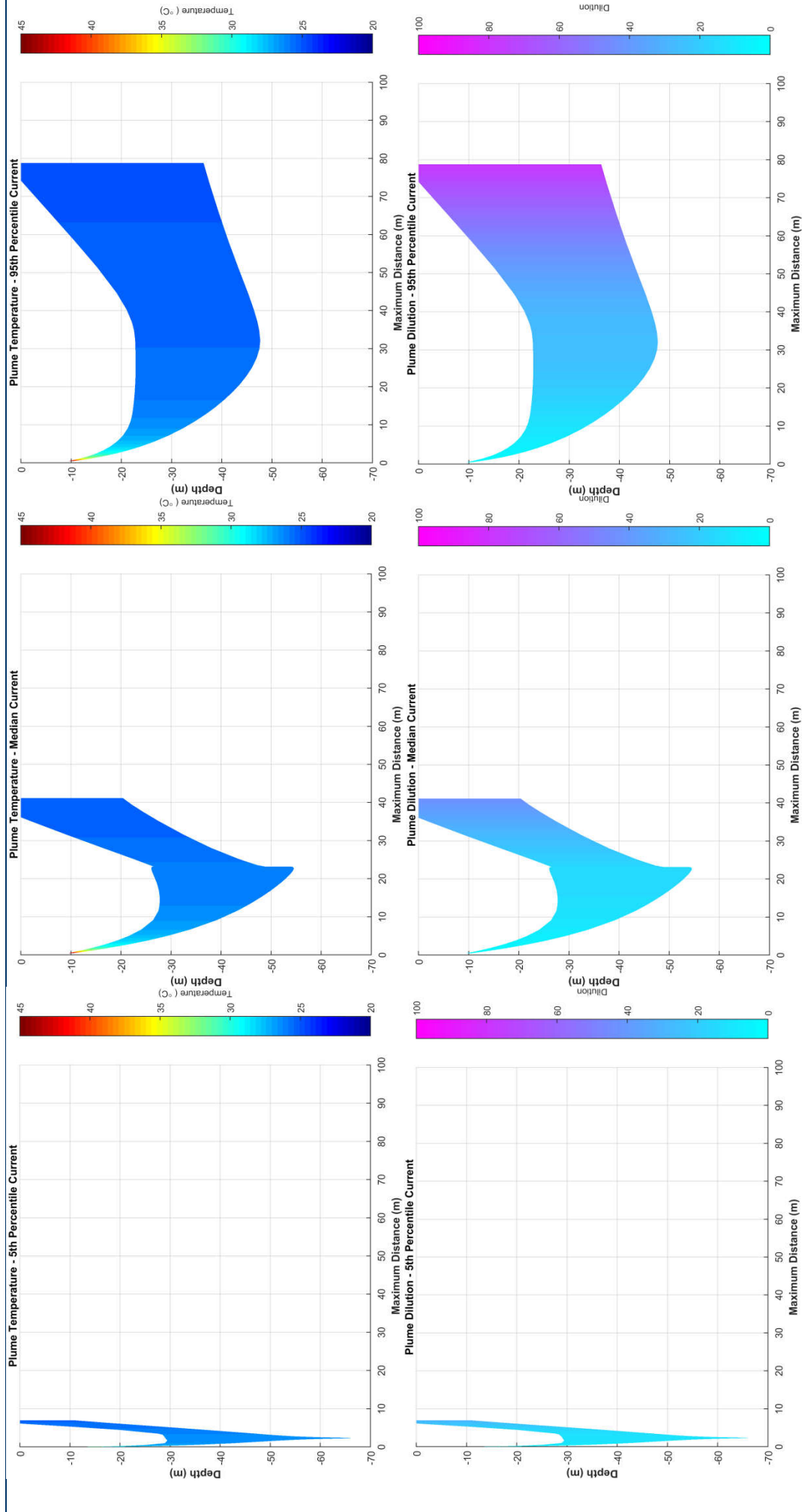
Figure 21 Near-field average temperature and dilution results for constant weak, medium and strong transitional currents for the maximum flow rate (360,576 m³/d)
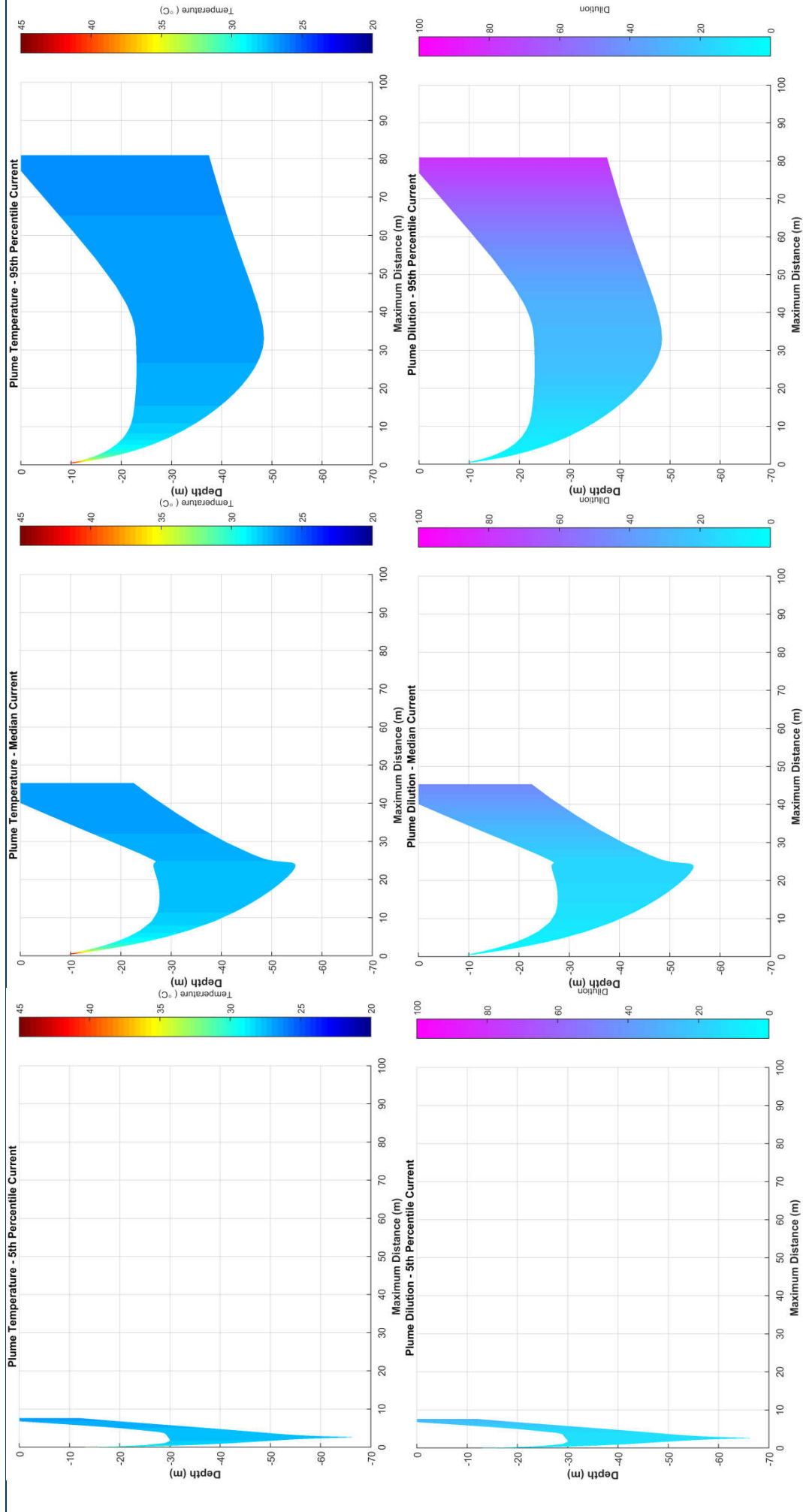
**Figure 22 Near-field average temperature and dilution results for constant weak, medium and strong winter currents for the maximum flow rate (360,576 m³/d)**

Table 8 Predicted plume characteristics upon encountering the sea surface (end of near-field mixing) for the minimum flow rate (288,000 m³/d flow) for each season and current speed.

Season	Surface current speed (m/s)	Plume diameter at the sea surface (m)	Plume temperature (°C)	Difference between plume and ambient temperature (°C)	Dilution of the plume (1:x)		Maximum horizontal distance (m)
					Minimum	Average	
Summer	Weak (0.04)	18.6	26.2	0.8	13	26	2.8
	Medium (0.11)	24.8	25.9	0.5	18	36	20.0
	Strong (0.27)	36.5	25.7	0.3	31	57	41.5
Transitional	Weak (0.05)	17.6	25.5	0.8	13	24	5.6
	Medium (0.14)	24.5	25.2	0.5	17	37	33.6
	Strong (0.29)	32.3	25.0	0.3	20	66	64.7
Winter	Weak (0.03)	18.2	27.0	0.7	13	25	6.2
	Medium (0.11)	26.0	26.8	0.5	19	40	37.2
	Strong (0.27)	33.1	26.6	0.3	21	69	67.1

Table 9 Predicted plume characteristics upon encountering the sea surface (end of near-field mixing) for the maximum flow rate (360,576 m³/d) for each season and current speed.

Season	Surface current speed (m/s)	Plume diameter at the sea surface (m)	Plume temperature (°C)	Difference between plume and ambient temperature (°C)	Dilution of the plume (1:x)		Maximum horizontal distance (m)
					Minimum	Average	
Summer	Weak (0.04)	22.8	26.3	0.6	16	31	4.3
	Medium (0.11)	29.3	25.9	0.5	21	41	25.7
	Strong (0.27)	43.0	25.7	0.3	43	65	55.0
Transitional	Weak (0.05)	21.6	25.4	0.7	15	30	7.0
	Medium (0.14)	29.8	25.2	0.5	20	44	41.2
	Strong (0.29)	39.4	25.0	0.3	24	78	78.8
Winter	Weak (0.03)	22.2	26.9	0.6	16	30	7.7
	Medium (0.11)	31.44	26.7	0.4	22	47	45.4
	Strong (0.27)	40.1	26.5	0.2	25	80	81.0

3.2 Far-field modelling

3.2.1 General observations

Figure 23 and Figure 24 show screenshots of predicted concentrations (and equivalent dilutions) for the chlorine every 2 hours from 4 am to 2 pm 1st September 2012. The results are based on the minimum flow rate of 288,000 m^3/d.

The images have been included to illustrate that the concentrations (and in turn dilutions) became more variable over time as a result of the change in current directions and speeds. Lower concentrations (higher dilution rates) occurred during stronger currents, whereas patches of higher concentrations (lower dilution rates) tended to build up at the turn of the tide or during weaker current events. Additionally, during these periods of decreased current speeds the predicted plume typically demonstrated a more continuous appearance, with the higher concentration patches moving as a unified group.
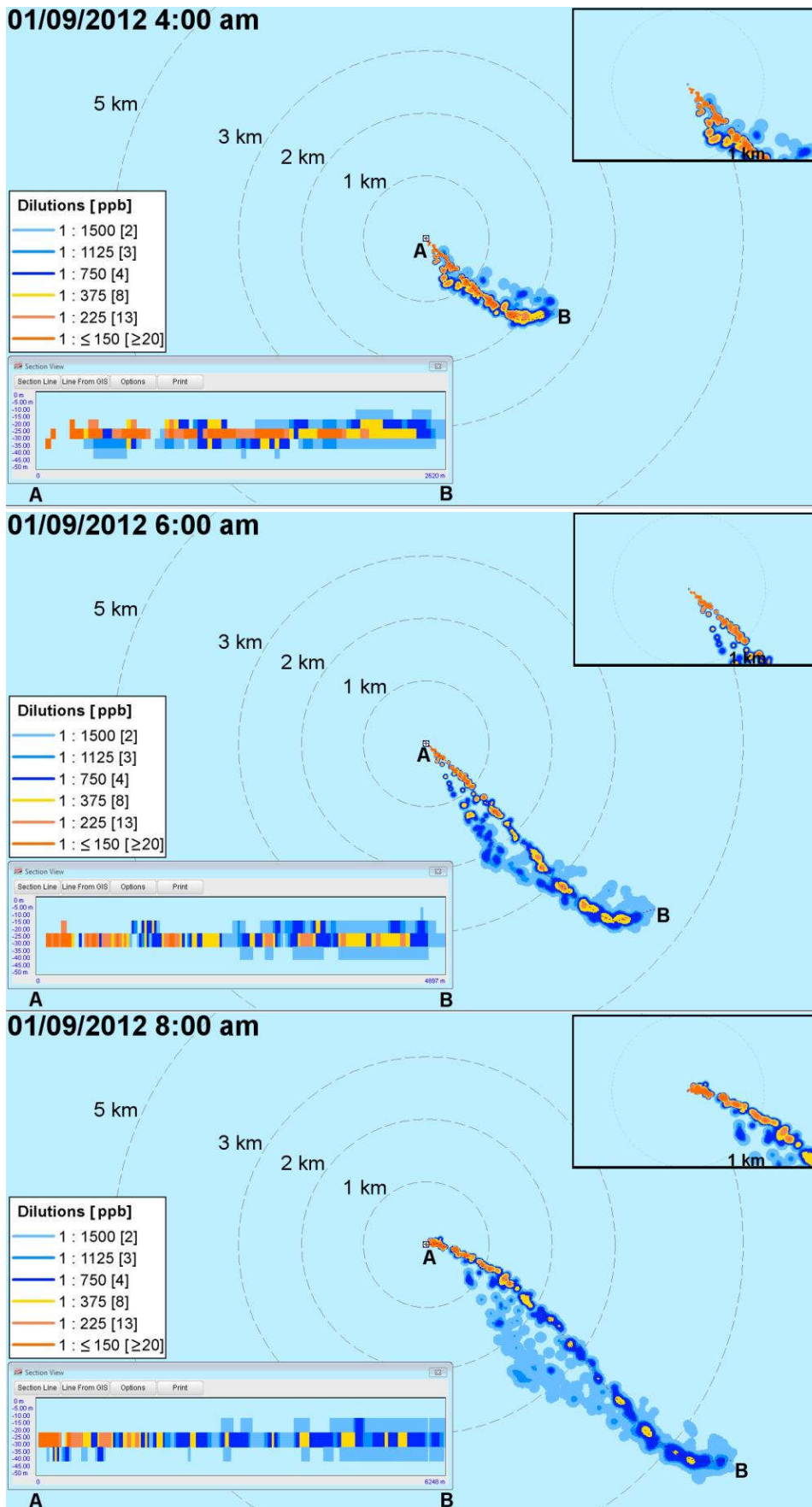
Figure 23 Screenshot every 2 hours of the predicted chlorine concentration (and equivalent dilution) from 4 am to 8 am 1st September 2012. Results are based on the maximum water column concentration for the maximum flow rate scenario (288,000 m³/d). Figure insets illustrate zoomed-in view of predicted plume concentrations.
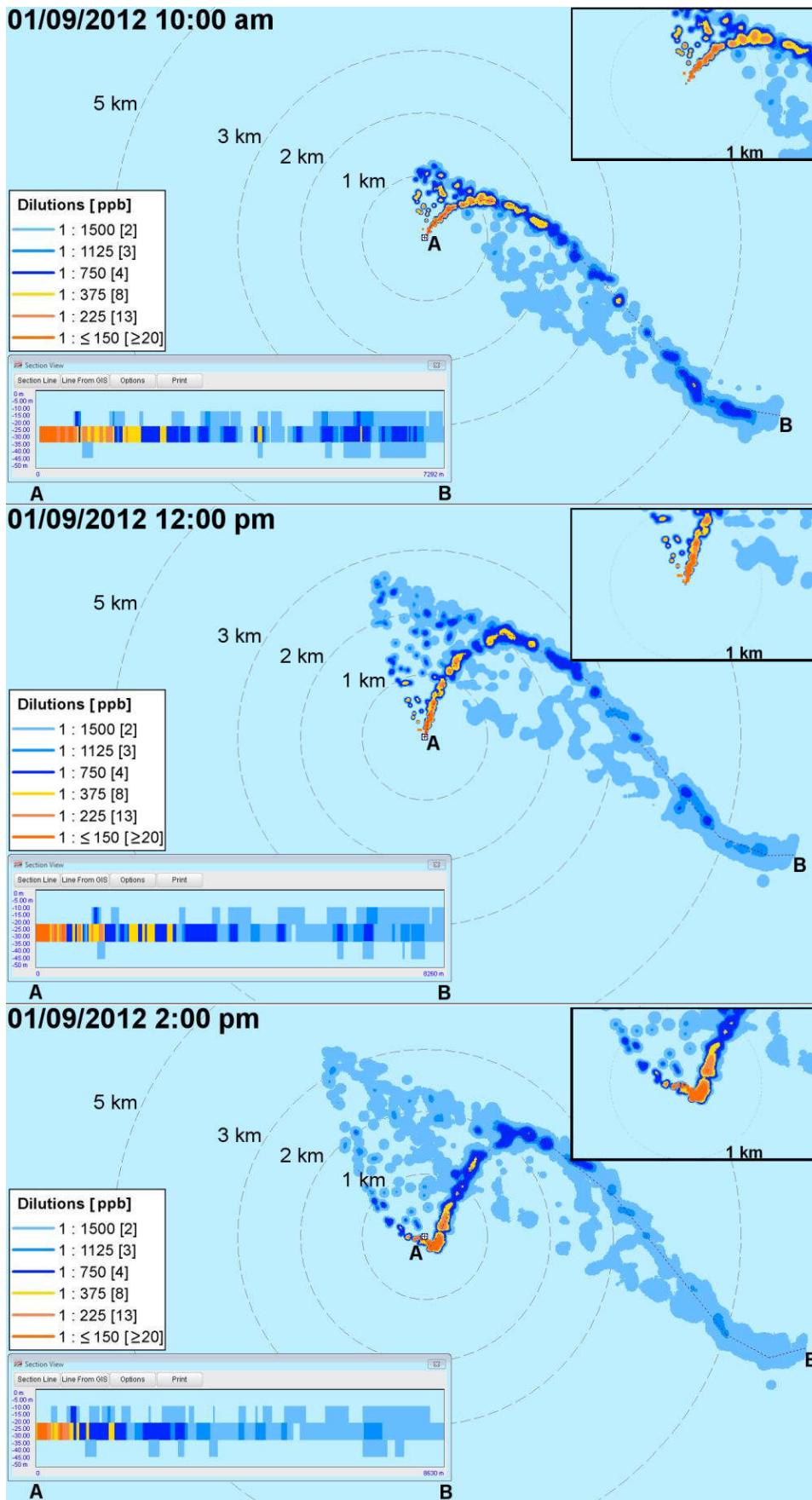
Figure 24 Screenshot every 2 hours of the predicted chlorine concentration (and equivalent dilution) from 10 am to 2 pm 1st September 2012. Results are based on the maximum water column concentration for the maximum flow rate scenario (288,000 m³/d). Figure insets illustrate zoomed-in view of predicted plume concentrations.

3.2.2   Seasonal analysis

The 15 minute model outputs for each month from each of the three years (2010, 2012 and 2014) were combined and analysed according to the respective season (i.e. summer – December, January, February; transitional periods – March, April and September to November; and winter – May to August). This approach assists with identifying the potential for exposure on a seasonal basis, to the nearest shoals/banks (i.e. Evans Shoal, Tassie Shoal and Lynedoch Bank) whilst taking into account the interannual variability.

Table 10 shows the chlorine concentrations achieved at specific distances from the release location for each flow rate and season.

Table 11 is a summary of the maximum distances from release site to achieve a given concentration for each flow rate and season. For both flow rates and all three seasons, 13 ppb (which represents the predicted no effect concentration for acute exposure based on Chariton and Stauber (2008)) was achieved within 4.6 km from the release location. The maximum distance to achieve 2 ppb (which represents the predicted no effect concentration in the event of chronic exposure to chlorine at the 99% species protection level, as reported by CSIRO (Chariton and Stauber 2008)) was 20.51 km from the release location. Based on the distance from the 13 ppb and 2 ppb chlorine concentration contours to the closest shoal/bank being Evans Shoal (minimum distance of approximately 62.49 km and 53.37 km, respectively) no exposure is expected for non-transient species and receptors.

Table 12 presents the total area of coverage for a given chlorine concentration for each flow rate and season. Based on the minimum flow rate (288,000 m^3/d) and ≥13 ppb concentration, the total area of coverage was largest during the transitional months (19.50 km^2) and smallest during the summer months (18.92 km^2). The extent was found to be influenced by the rate of discharge. For example, by increasing the flow rate to 360,576 m^3/d and maintaining the initial chlorine concentration of 3,000 ppb, the ≥13 ppb area of coverage increased by 60% for the summer conditions (from 18.92 km^2 to 30.43 km^2). The maximum extent of the ≥ 13 ppb area was 30.43 km^2. For ≥ 2 ppb and minimum flow rate, the area of coverage was largest during the summer conditions (313.06 km^2). When assessing the maximum flow rate, the ≥ 2 ppb area of coverage increased by approximately 22% for the summer conditions (366.42 km^2).

The predicted extents of the chlorine concentrations (and minimum dilutions) for each season and flow rate (288,000 m^3/d and 360,576 m^3/d), assuming an initial chlorine concentration of 1,000 ppb, are shown in Figure 25 to Figure 30. Note that the images represent the highest chlorine concentration at any given time-step through the water column and does not take into account frequency or duration.

Table 10 Chlorine concentrations achieved at specific distances from the cooling water discharge release location for each flow rate and season

Flow rate (m³/d)	Season	Maximum chlorine concentrations (ppb) achieved at specific distances from the release location						
		0.1 km radius	0.5 km radius	1 km radius	2 km radius	3 km radius	5 km radius	> 5 km radius
288,000	Summer	≥ 20	≥ 20	≥ 20	13	13	4	2
	Transitional	≥ 20	≥ 20	≥ 20	13	13	2	2
	Winter	≥ 20	≥ 20	≥ 20	13	13	2	2
360,576	Summer	≥ 20	≥ 20	≥ 20	13	13	8	2
	Transitional	≥ 20	≥ 20	≥ 20	13	13	2	2
	Winter	≥ 20	≥ 20	≥ 20	13	13	4	2

Table 11 Maximum distance from the release location to achieve a given chlorine concentration for each flow rate and season

Flow rate (m³/d)	Season	Maximum distance (km) from release location to achieve chlorine concentrations (ppb)					
		≥ 20	13	8	4	3	2
288,000	Summer	2.36	3.55	5.27	9.76	11.87	18.99
	Transitional	2.74	3.51	4.84	10.17	12.89	19.30
	Winter	2.49	3.58	5.15	9.67	11.97	19.22
360,576	Summer	3.32	4.55	5.70	10.23	12.90	19.94
	Transitional	3.00	3.97	6.37	11.57	18.61	20.51
	Winter	3.11	4.60	5.79	10.41	16.29	20.03

Table 12 Total area of coverage for a given chlorine concentration for each flow rate and season

Flow rate (m³/d)	Season	Total area (km²) of coverage for assigned chlorine concentrations (ppb)					
		≥ 20	≥ 13	≥ 8	≥ 4	≥ 3	≥ 2
288,000	Summer	4.63	18.92	47.52	119.17	177.52	313.06
	Transitional	6.69	19.50	41.94	125.43	187.80	300.45
	Winter	5.54	17.66	40.77	118.67	190.41	310.39
360,576	Summer	11.87	30.43	60.30	158.01	249.05	343.03
	Transitional	12.82	29.01	60.90	166.51	254.33	366.42
	Winter	11.47	27.83	56.88	166.72	263.04	331.70
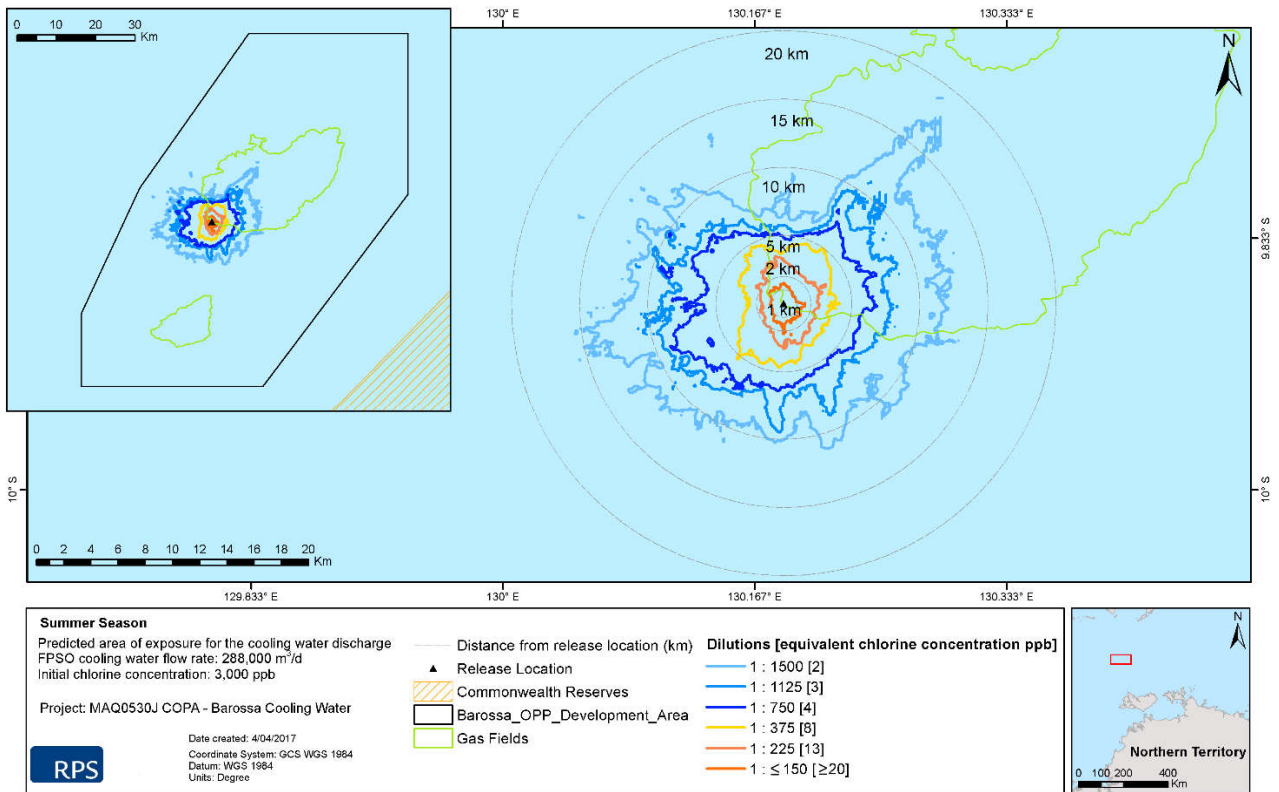
Figure 25 Predicted area of exposure by chlorine under summer conditions for the minimum cooling water flow rate (288,000 m³/d)
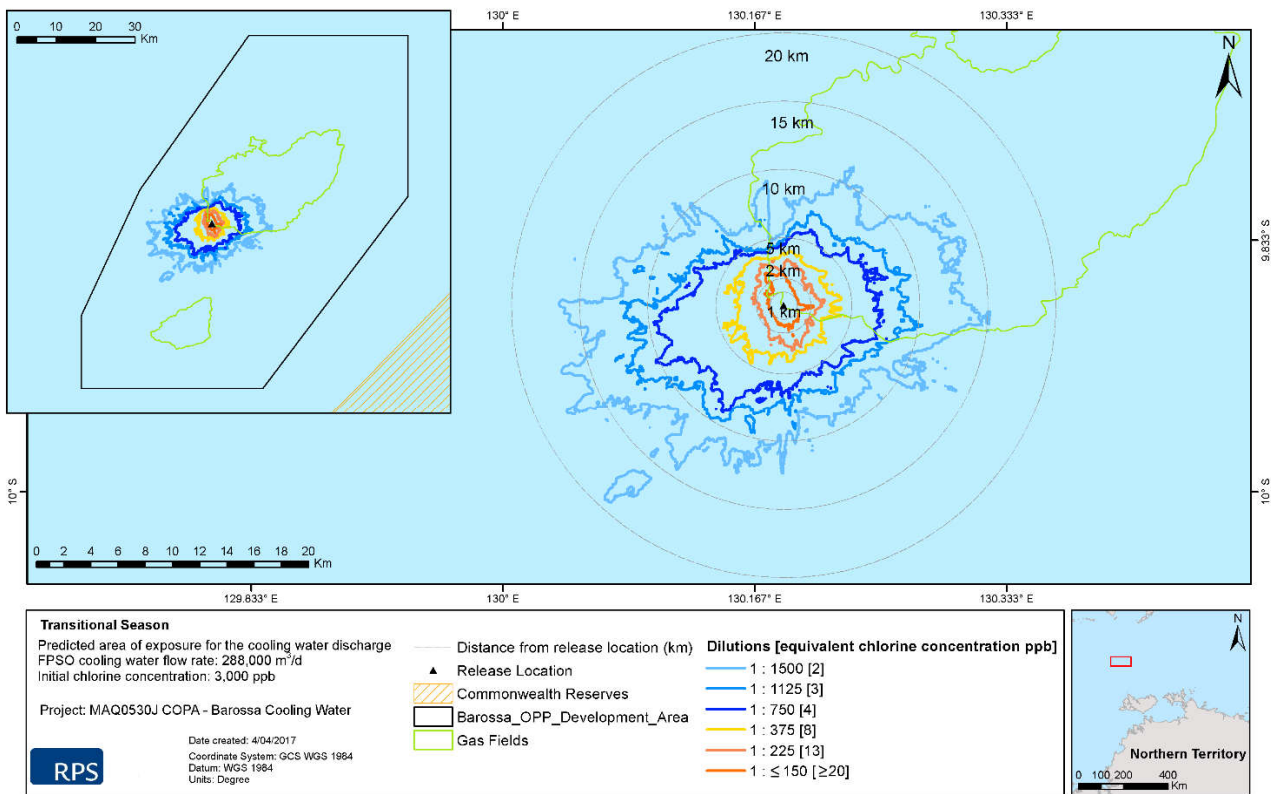
Figure 26 Predicted area of exposure by chlorine under transitional conditions for the minimum cooling water flow rate (288,000 m³/d)
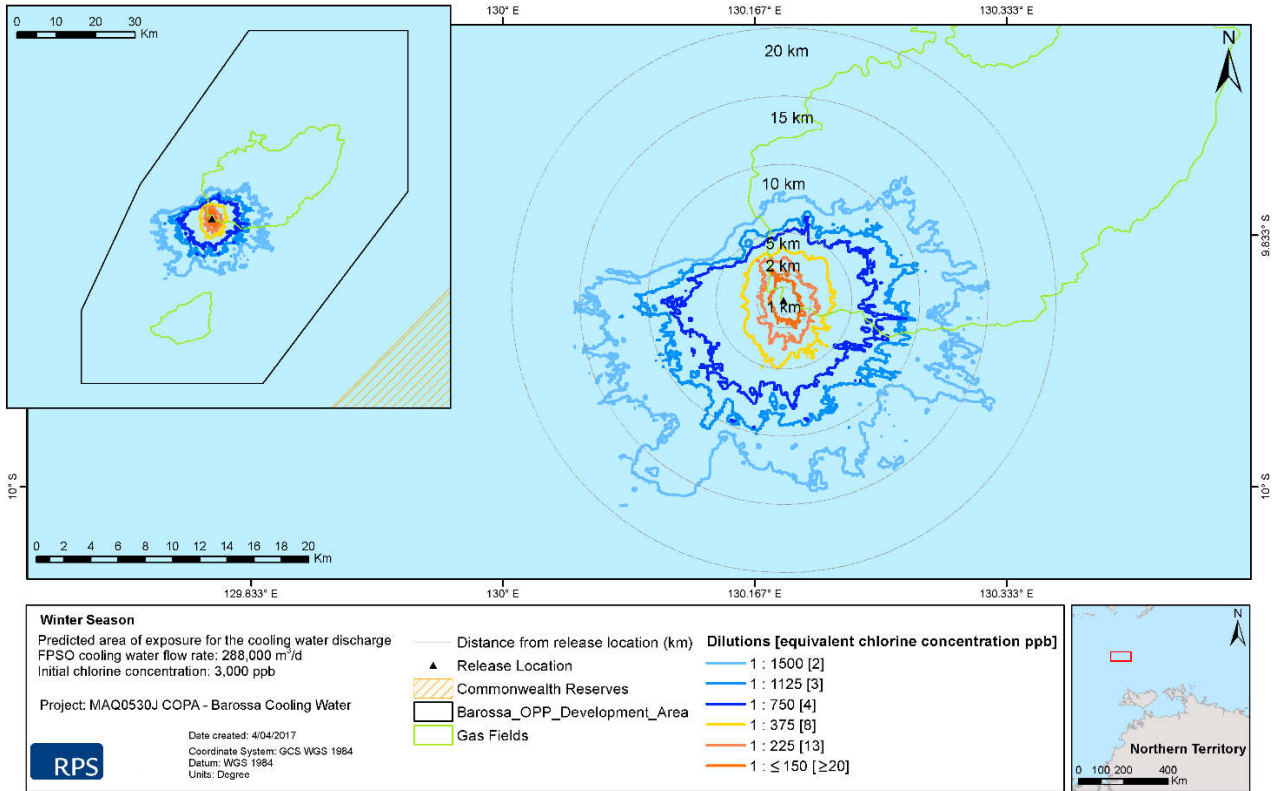
Figure 27 Predicted area of exposure by chlorine under winter conditions for the minimum cooling water flow rate (288,000 m³/d)
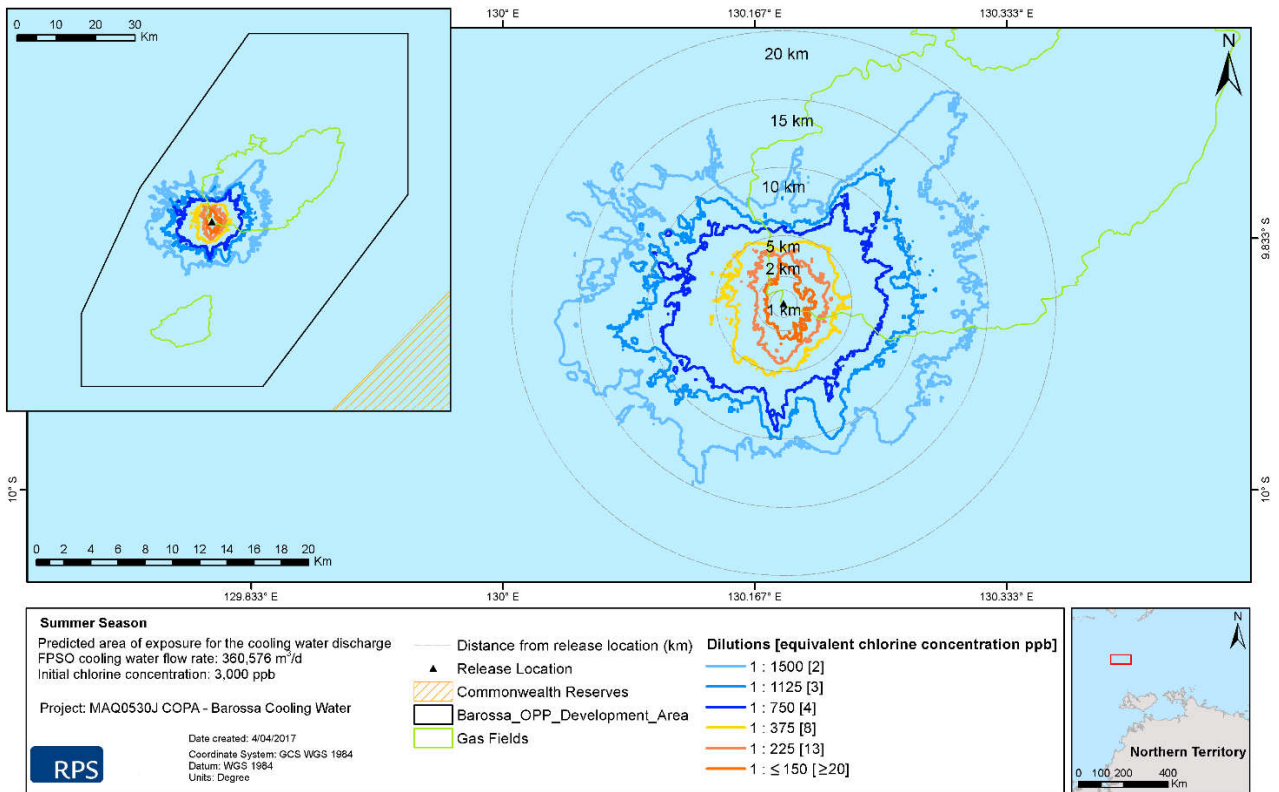
Figure 28 Predicted area of exposure by chlorine under summer conditions for the maximum cooling water flow rate (360,576 m³/d)
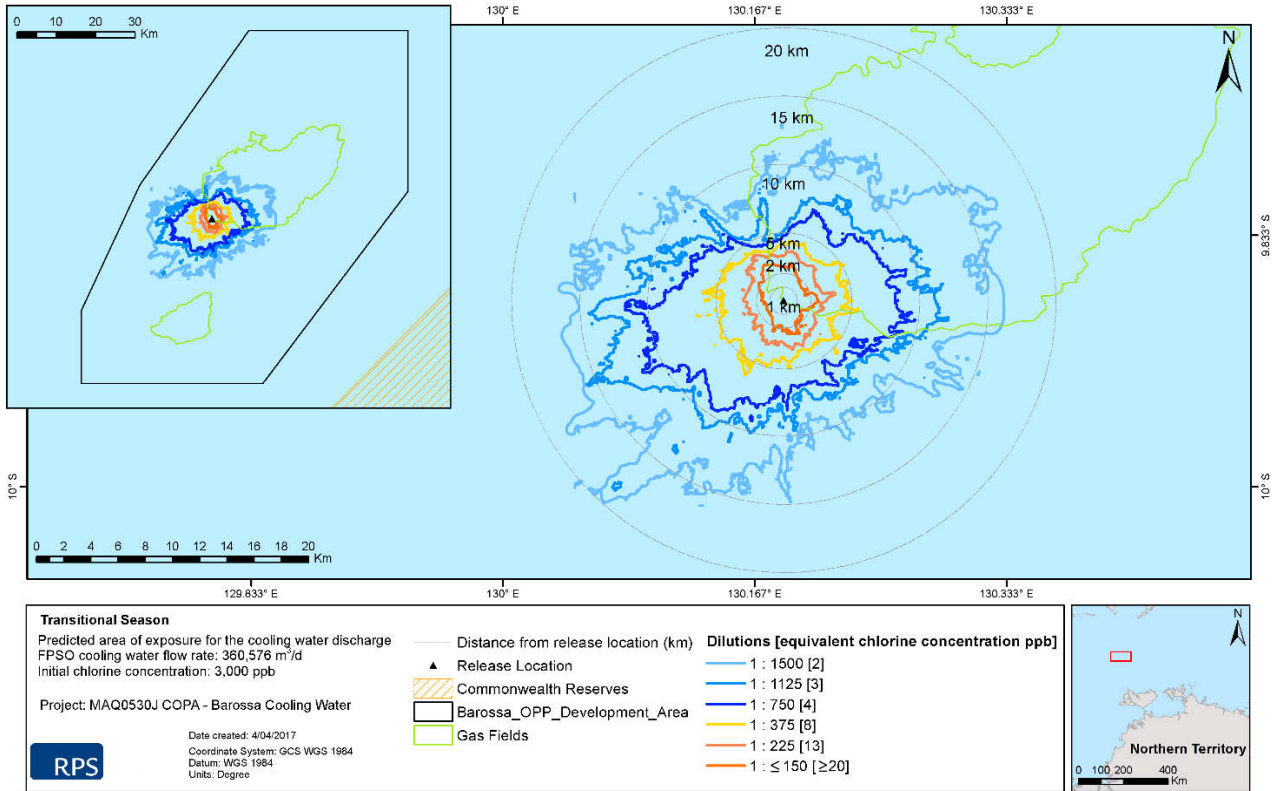
Figure 29 Predicted area of exposure by chlorine under transitional conditions for the maximum cooling water flow rate (360,576 m³/d)
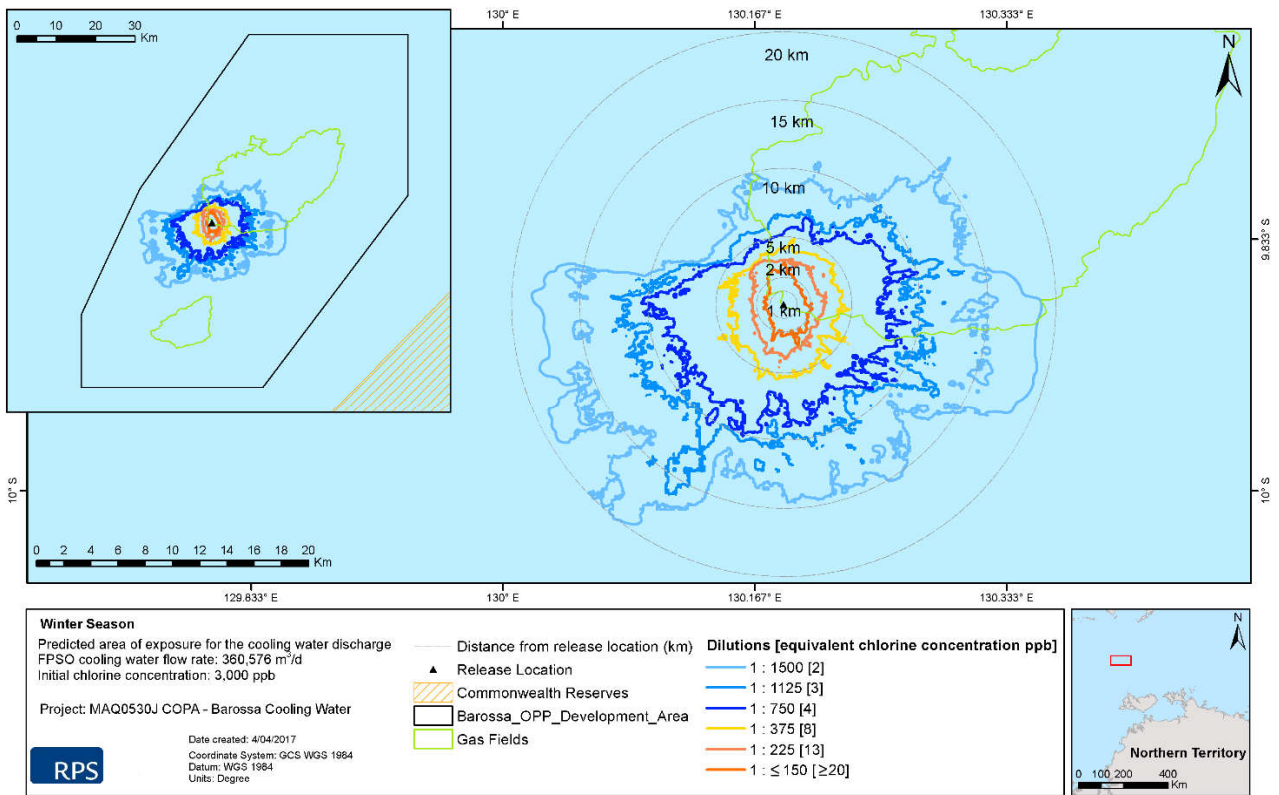

Figure 30 Predicted area of exposure by chlorine under winter conditions for the maximum cooling water flow rate (360,576 m³/d)

3.2.3 Combined analysis

Table 13 shows the maximum distance from the release location to achieve chlorine concentrations for each flow rate. The 13 ppb contour was predicted to be 3.58 km and 4.60 km from the release location for the minimum and maximum flow rate, respectively. Whereas, the 2 ppb zone was predicted to extend up to 19.33 km and 20.51 km from the release location for the minimum and maximum flow rate, respectively.

Table 14 shows the total area of coverage for a given chlorine concentration for each flow rate. Based on the maximum flow rate and ≥ 2 ppb , the area of coverage was 420.18 km^2, which was approximately 12% larger, compared to the results for the minimum flow rate (376.16 km^2).

Figure 31 and Figure 32 present the predicted residual chlorine concentrations (and minimum dilutions) based on combined results for 2010, 2012 and 2014 conditions for the minimum and maximum cooling water flow rates, respectively.

Table 13 Maximum distance from cooling water discharge release location to achieve chlorine concentrations for each flow rate

Flow rate (m^3/d)	Maximum distance (km) from release location to achieve chlorine concentrations (ppb)					
	≥ 20	≥ 13	≥ 8	≥ 4	≥ 3	≥ 2
288,000	2.74	3.58	5.27	10.17	12.89	19.30
360,576	3.32	4.60	6.37	11.57	18.61	20.51

Table 14 Total area of coverage for given chlorine concentrations for each flow rate

| Flow rate (m^3/d)	Total area (km^2) of coverage for assigned chlorine concentrations (ppb)					
	≥ 20	≥ 13	≥ 8	≥ 4	≥ 3	≥ 2
288,000	7.63	22.26	52.37	148.30	232.77	376.21
360,576	15.37	33.99	72.60	204.85	327.35	420.18
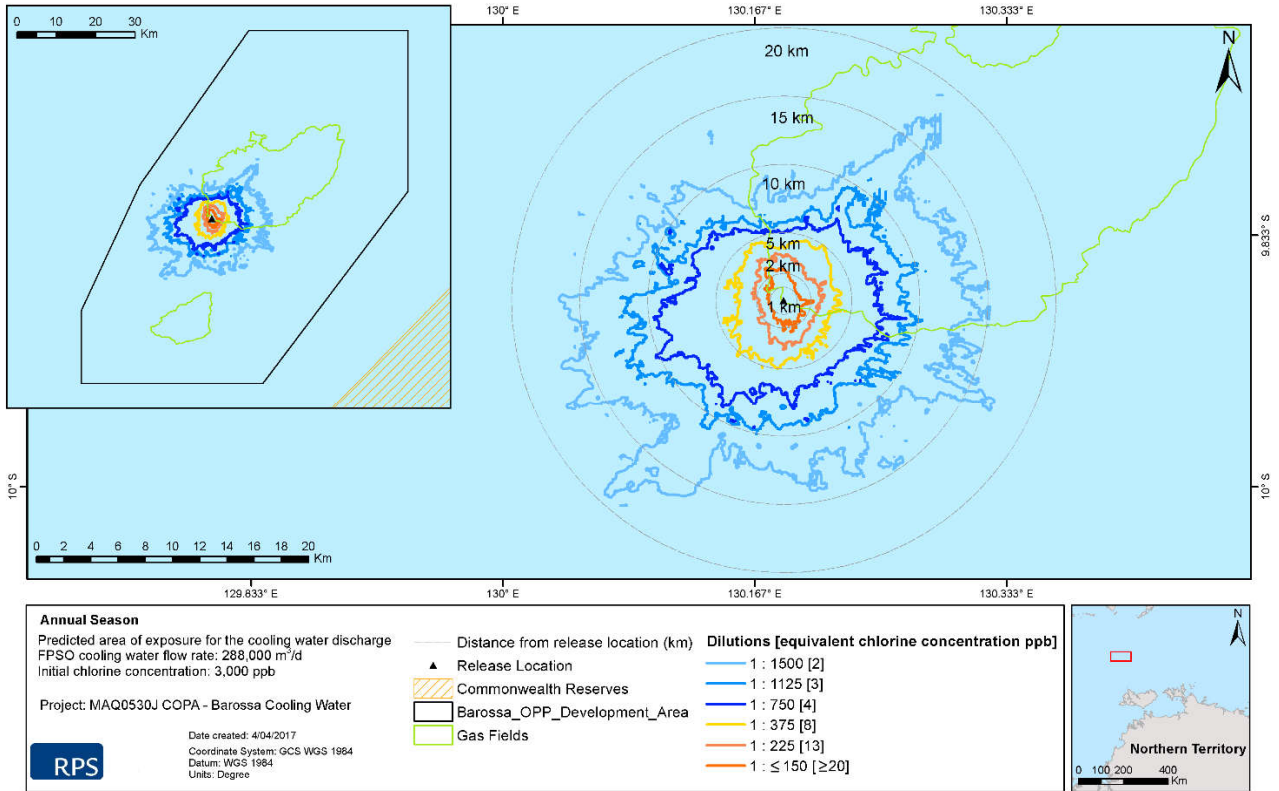
Figure 31 Predicted area of exposure by chlorine based on the minimum cooling water flow rate (288,000 m³/d)
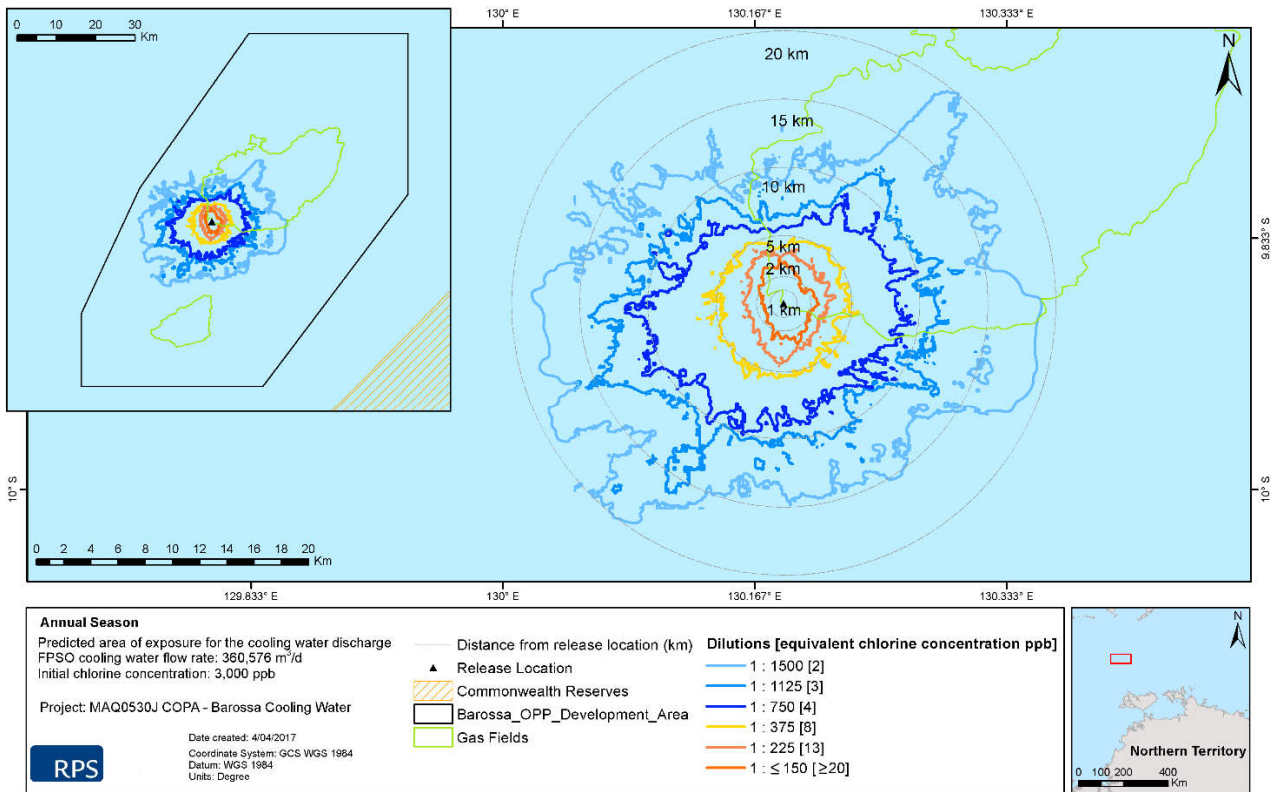

Figure 32 Predicted area of exposure by chlorine based on the maximum cooling water flow rate (360,576 m³/d)

4.0   References

Andersen, O.B. 1995. 'Global ocean tides from ERS 1 and TOPEX/POSEIDON altimetry'. Journal of Geophysical Research: Oceans, vol. 100, no. C12, pp. 25249–25259.

Australian Bureau of Meteorology. 2015. The Southern Oscillation Index – Monthly Southern Oscillation Index. viewed 28 September 2015, ftp://ftp.bom.gov.au/anon/home/ncc/www/sco/soi/soiplaintext.html.

Baumgartner, D., Frick, W. and Roberts, P. 1994. Dilution models for Effluent Discharges, U.S. Environment Protection Agency, Newport.

Carvalho, J.L.B., Roberts, P.J.W. and Roldão, J. 2002. 'Field Observations of the Ipanema Beach Outfall'. Journal of Hydraulic Engineering, vol. 128, no. 2, pp. 151–160.

Chariton, A.A. and Stauber, J.L. 2008. Toxicity of chlorine and its major by-products in seawater: a literature review. Commonwealth Scientific and Industrial Research Organisation Land and Water, Canberra, Australian Capital Territory.

Chassignet, E.P., Hurlburt, H.E., Smedstad, O.M., Halliwell, G.R., Hogan, P.J., Wallcraft, A.J., Baraille, R. and Bleck, R. 2007. 'The HYCOM (Hybrid Coordinate Ocean Model) data assimilative system'. Journal of Marine Systems, vol. 65, no. 1, pp. 60–83.

Chassignet, E., Hurlburt, H., Metzger, E., Smedstad, O., Cummings, J and Halliwell, G. 2009. 'U.S. GODAE: Global Ocean Prediction with the HYbrid Coordinate Ocean Model (HYCOM)'. Oceanography, vol. 22, no. 2, pp. 64–75.

Davies, A.M. 1977a. 'The numerical solutions of the three-dimensional hydrodynamic equations using a B-spline representation of the vertical current profile'. In: Nihoul, J.C. (ed). Bottom Turbulence: Proceedings of the 8th Liège Colloquium on Ocean Hydrodynamics. Elsevier Scientific, Amsterdam, pp. 1–25.

Davies, A.M. 1977b. 'Three-dimensional model with depth-varying eddy viscosity'. In: Nihoul, J.C. (ed). Bottom Turbulence: Proceedings of the 8th Liège Colloquium on Ocean Hydrodynamics. Elsevier Scientific, Amsterdam, pp. 27–48.

French McCay, D.P. and Isaji, T. 2004. 'Evaluation of the consequences of chemical spills using modeling: Chemicals used in deepwater oil and gas operations'. Environmental Modelling and Software, vol. 19, no. 7, pp. 629–644.

French McCay, D.P., Whittier, N., Ward, M. and Santos, C. 2006. 'Spill hazard evaluation for chemicals shipped in bulk using modelling'. Environmental Modelling and Software, vol. 21, no. 2, pp. 156–169.

Frick, W.E., Roberts, P.J.W., Davis, L.R., Keyes, J., Baumgartner, D.J. and George, K.P. 2003. Dilution Models for Effluent Discharges (Visual Plumes) 4th Edition. Ecosystems Research Division U.S. Environmental Protection Agency, Georgia.

Fu, R., Del Genio, A.D. and Rossow, W.B. 1994. 'Influence of ocean surface conditions on atmospheric vertical thermodynamic structure and deep convection'. Journal of Climate, vol.7, no. 7, pp. 1092–1108.

Fugro. 2015. Barossa Field Meteorological, Current Profile, Wave and CTD Measurements – Final Report. Reporting Period: 8 July 2014 to 16 July 2015. Unpublished report prepared for ConocoPhillips Australia Pty Ltd., Perth, Western Australia.

Gordon, R. 1982. 'Wind driven circulation in Narragansett Bay' PhD thesis. Department of Ocean Engineering, University of Rhode Island.

International Finance Corporation World Bank Group (IFC). 2015. IFC's Sustainability Framework – Industry Sector Guidelines: Environmental, Health and Safety Guidelines For Offshore Oil And Gas Development. Available at: http://www.ifc.org/wps/wcm/connect/f3a7f38048cb251ea609b76bcf395ce1/FINAL_Jun+2015_Offshore+Oil+and+Gas_EHS+Guideline.pdf?MOD=AJPERES (accessed 22 February 2017).

Isaji, T. and Spaulding, M. 1984. 'A model of the tidally induced residual circulation in the Gulf of Maine and Georges Bank'. Journal of Physical Oceanography, vol. 14, no. 6, pp. 1119–1126.

Isaji, T., Howlett, E., Dalton C., and Anderson, E. 2001. 'Stepwise-continuous-variable-rectangular grid hydrodynamics model', Proceedings of the 24th Arctic and Marine Oil Spill Program (AMOP) Technical Seminar (including 18th TSOCS and 3rd PHYTO). Environment Canada, Edmonton, pp. 597–610.

Kostianoy, A.G., Ginzburg, A.I., Lebedev, S.A., Frankignoulle, M. and Delille, B. 2003. 'Fronts and mesoscale variability in the southern Indian Ocean as inferred from the TOPEX/POSEIDON and ERS-2 Altimetry data'. Oceanology, vol. 43, no. 5, pp. 632–642.

Ludicone, D., Santoleri, R., Marullo, S. and Gerosa, P. 1998. 'Sea level variability and surface eddy statistics in the Mediterranean Sea from TOPEX/POSEIDON data. Journal of Geophysical Research, vol. 103, no. C2, pp. 2995–3011.

Matsumoto, K., Takanezawa, T. and Ooe, M. 2000. 'Ocean tide models developed by assimilating TOPEX/POSEIDON altimeter data into hydrodynamical model: A global model and a regional model around Japan'. Journal of Oceanography, vol. 56, no.5, pp. 567–581.

National Aeronautics and Space Administration (NASA). 2013a. National Aeronautics and Space Administration/Jet Propulsion Laboratory TOPEX/Poseidon Fact Sheet. NASA. Available at: https://sealevel.jpl.nasa.gov/missions/topex/topexfactsheet (accessed 23 November 2013).

National Aeronautics and Space Administration (NASA). 2013b. National Aeronautics and Space Administration/Jet Propulsion Laboratory TOPEX/Poseidon. NASA. Available at: https://sealevel.jpl.nasa.gov/missions/topex (accessed 23 November 2013).

Owen, A. 1980. 'A three-dimensional model of the Bristol Channel'. Journal of Physical Oceanography, vol. 10, no. 8, pp. 1290–1302.

Philander, S.G. 1990. El Niño, La Niña, and the Southern Oscillation. Academic Press, San Diego.

Qiu, B. and Chen, S. 2010. 'Eddy-mean flow interaction in the decadally modulating Kuroshio Extension system'. Deep-Sea Research II, vol. 57, no. 13, 1098–1110.

Rasmusson, E.M. and Wallace, J.M. 1983. 'Meteorological aspects of the El Niño/southern oscillation'. Science, vol. 222, no. 4629, pp. 1195–1202.

Roberts, P. and Tian, X. 2004. 'New experimental techniques for validation of marine discharge models'. Environmental Modelling and Software, vol. 19, no. 7, pp. 691–699.

RPS Asia-Pacific Applied Science Associates (RPS APASA). 2015. Potential Barossa Development, Hydrodynamic Model Comparison with Field Measurements. Unpublished report prepared for ConocoPhillips Australia Pty Ltd., Perth, Western Australia.

Shams El Din, A.M., Arain, R.A. and Hammoud, A.A. 2000. 'On the chlorination of seawater'. Desalination, vol. 129, no. 1, pp. 53–62.

Walstra, D.J.R., Van, Rijn, L.C., Blogg, H. and Van Ormondt, M. 2001. Evaluation of a hydrodynamic area model based on the COAST3D data at Teignmouth 1999. HR Wallingford, United Kingdom.

Woodside Energy Limited. 2011. Browse LNG Development, Draft Upstream Environmental Impact Statement, EPBC Referral 2008/4111, November 2011.

Yaremchuk, M. and Tangdong, Q. 2004. 'Seasonal variability of the large-scale currents near the coast of the Philippines'. Journal of Physical Oceanography, vol. 34, no., 4, pp. 844–855.

Zeng, J., Jiang, Z., Chen, Q., Zheng, P., Huang, Y. 2009. 'The decay kinetics of residual chlorine in cooling seawater simulation experiments'. Acta Oceanologica Sinica, vol. 28, no. 2, pp. 54-59.

Zigic, S., Zapata, M., Isaji,T., King, B. and Lemckert, C. 2003. 'Modelling of Moreton Bay using an ocean/coastal circulation model'. Proceedings of the 16th Australasian Coastal and Ocean Engineering Conference, the 9th Australasian Port and Harbour Conference and the Annual New Zealand Coastal Society Conference, Institution of Engineers Australia, Auckland, paper 170.

5.0　Appendices

Appendix A. Predicted plume temperature and distance plots for 288,000 m^3/d flow rate

Figure 33 to Figure 35 illustrate the predicted difference in plume and ambient sea surface temperature versus distance from the release location for the minimum flow rate (288,000 m^3/d) under weak, medium and strong current strengths and seasonal conditions.

5.0　Appendices
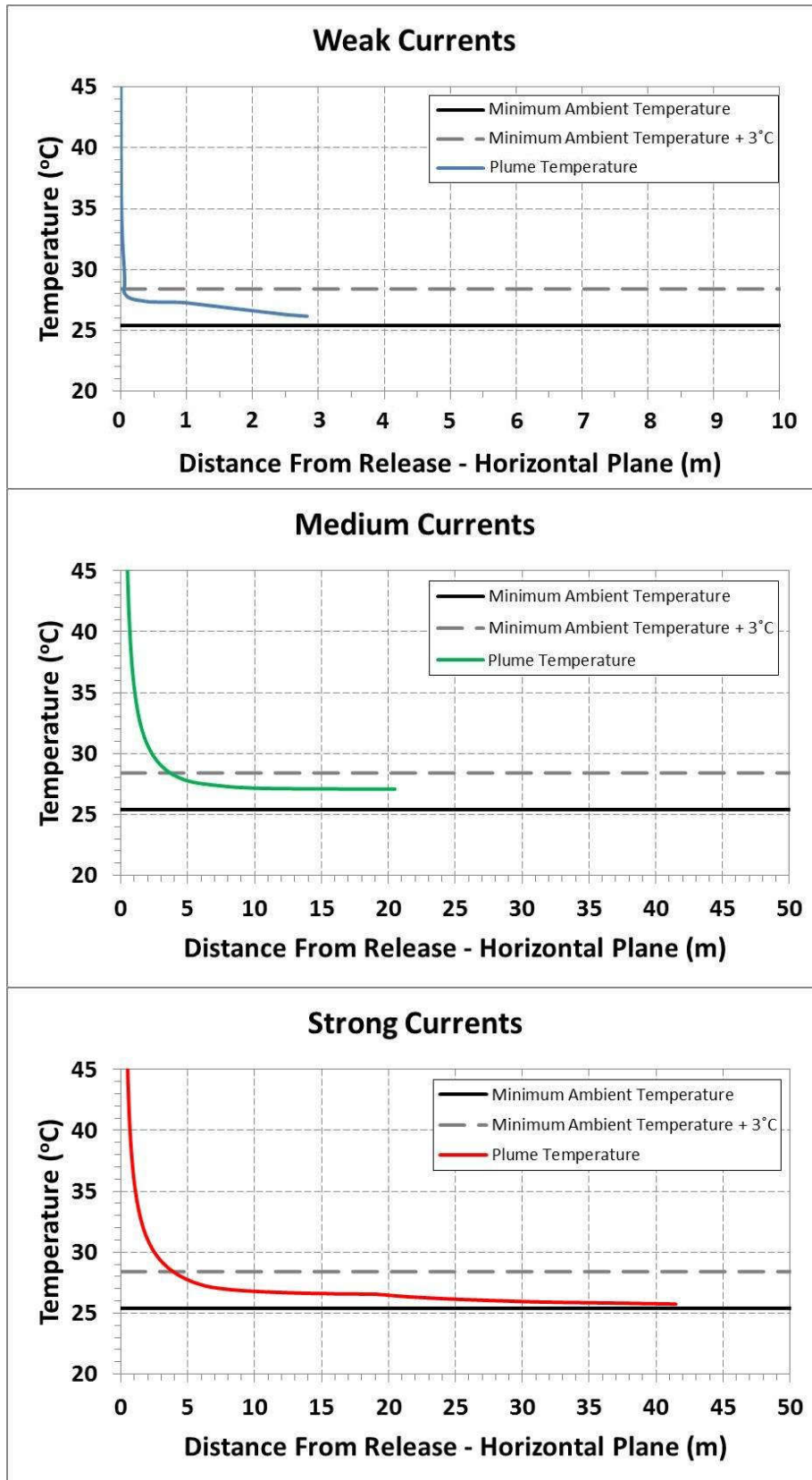
Figure 33 Predicted change in cooling water plume temperature as a function of distance from release location under weak, medium and strong current strengths during summer conditions (288,000 m³/d)
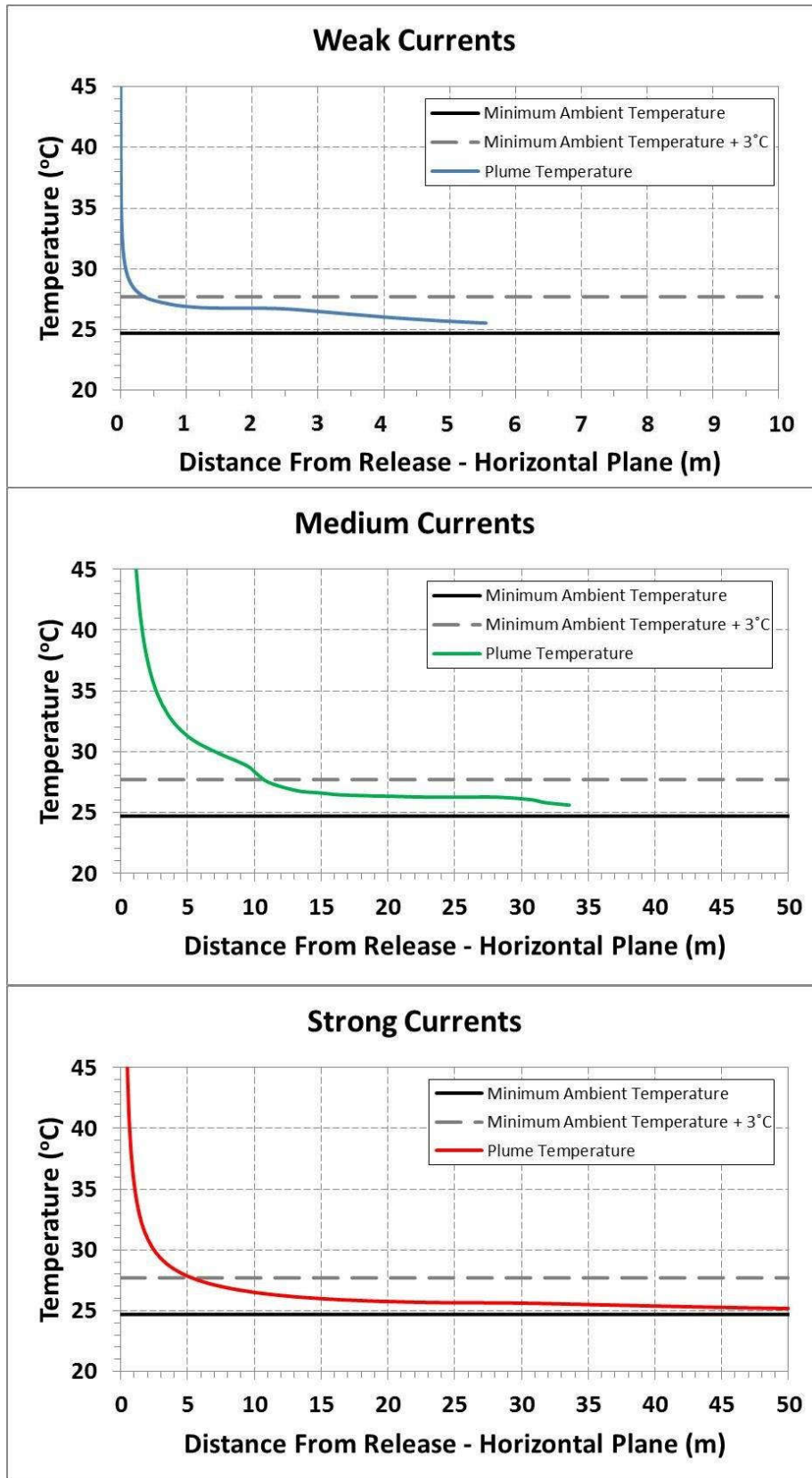
Figure 34 Predicted change in cooling water plume temperature as a function of distance from release location under weak, medium and strong current strengths during transitional conditions (288,000 m³/d)
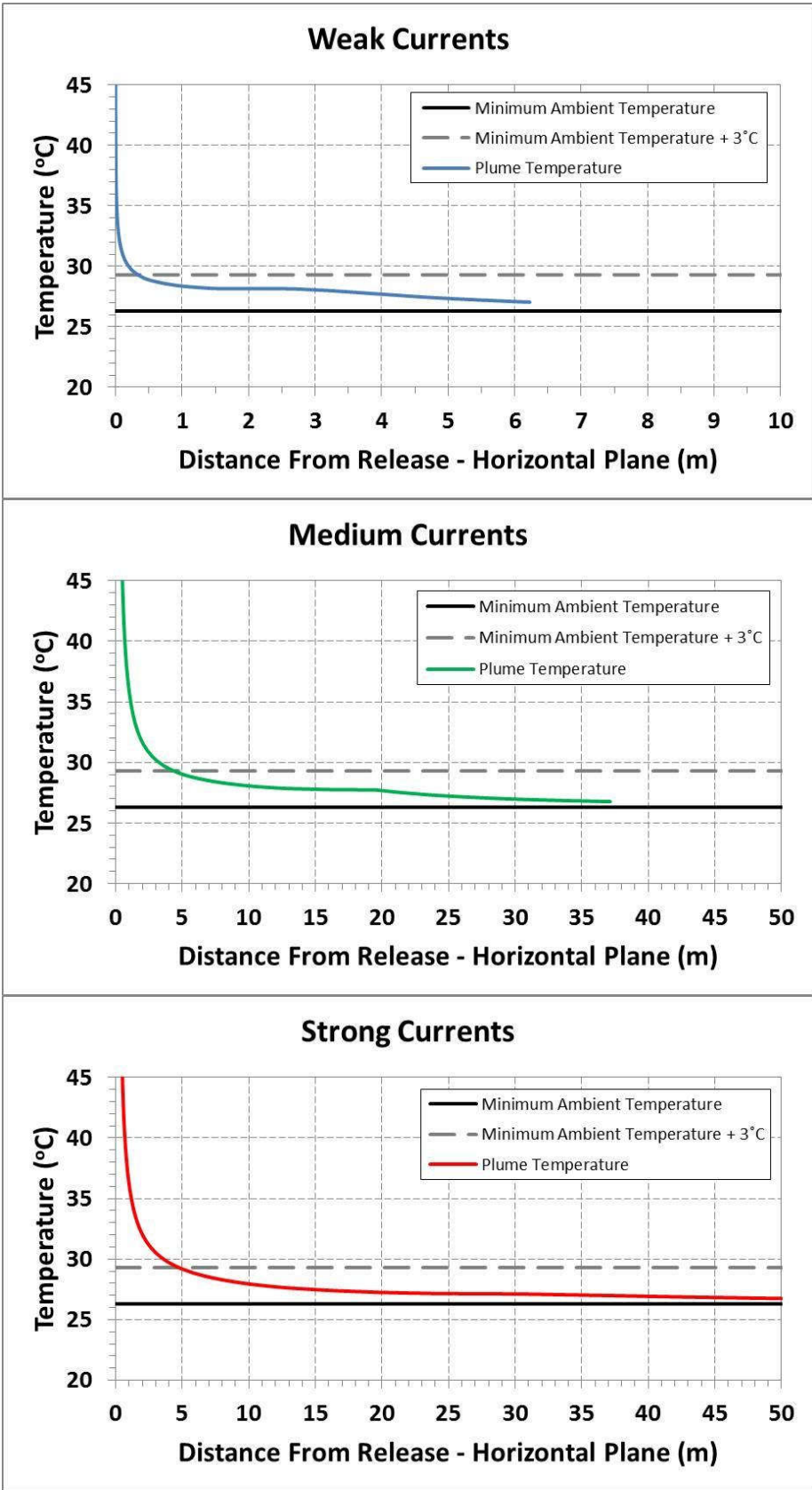
Figure 35 Predicted change in cooling water plume temperature as a function of distance from release location under weak, medium and strong current strengths during winter conditions (288,000 m³/d)

Appendix B. Predicted plume temperature and distance plots for 360,576 m³/d flow rate

Figure 36 to Figure 38 illustrate the predicted difference in plume and ambient sea surface temperature versus distance from release location for the maximum flow rate (360,576 m³/d) weak, medium and strong current strengths and seasonal conditions.
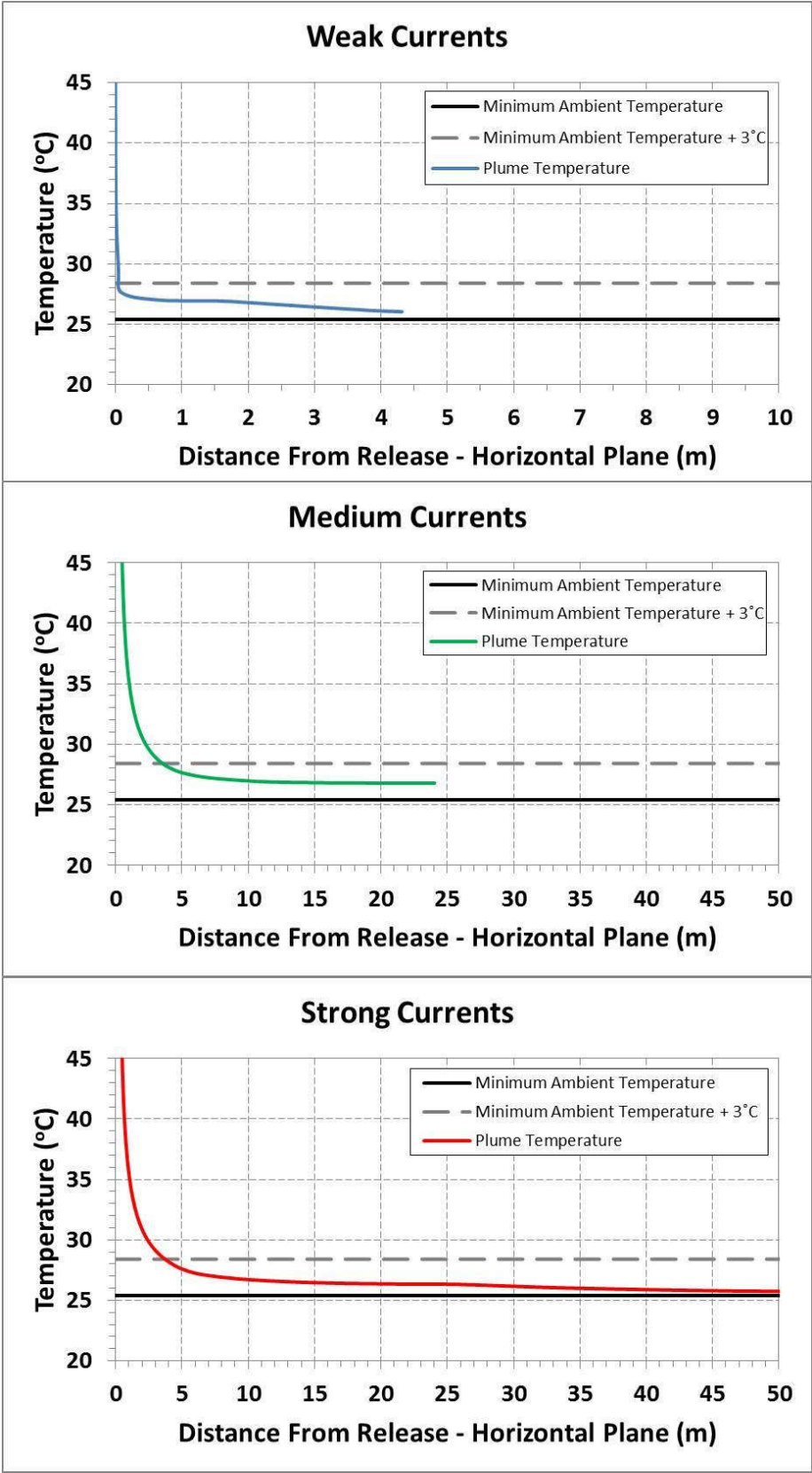
Figure 36 Predicted change in cooling water plume temperature as a function of distance from release location under weak, medium and strong current strengths during summer conditions (360,576 m³/d)
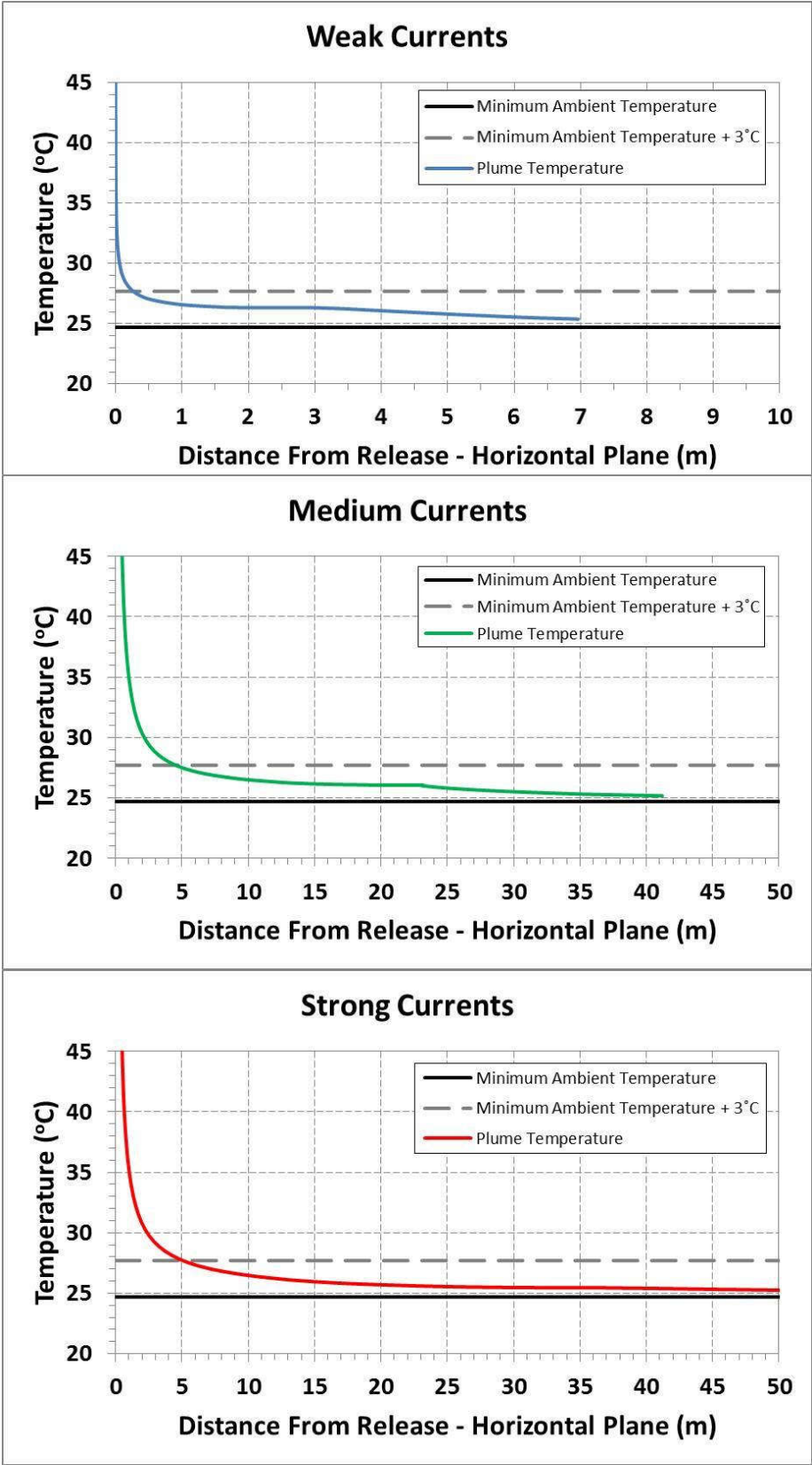
Figure 37 Predicted change in cooling water plume temperature as a function of distance from release location under weak, medium and strong current strengths during transitional conditions (360,576 m³/d)
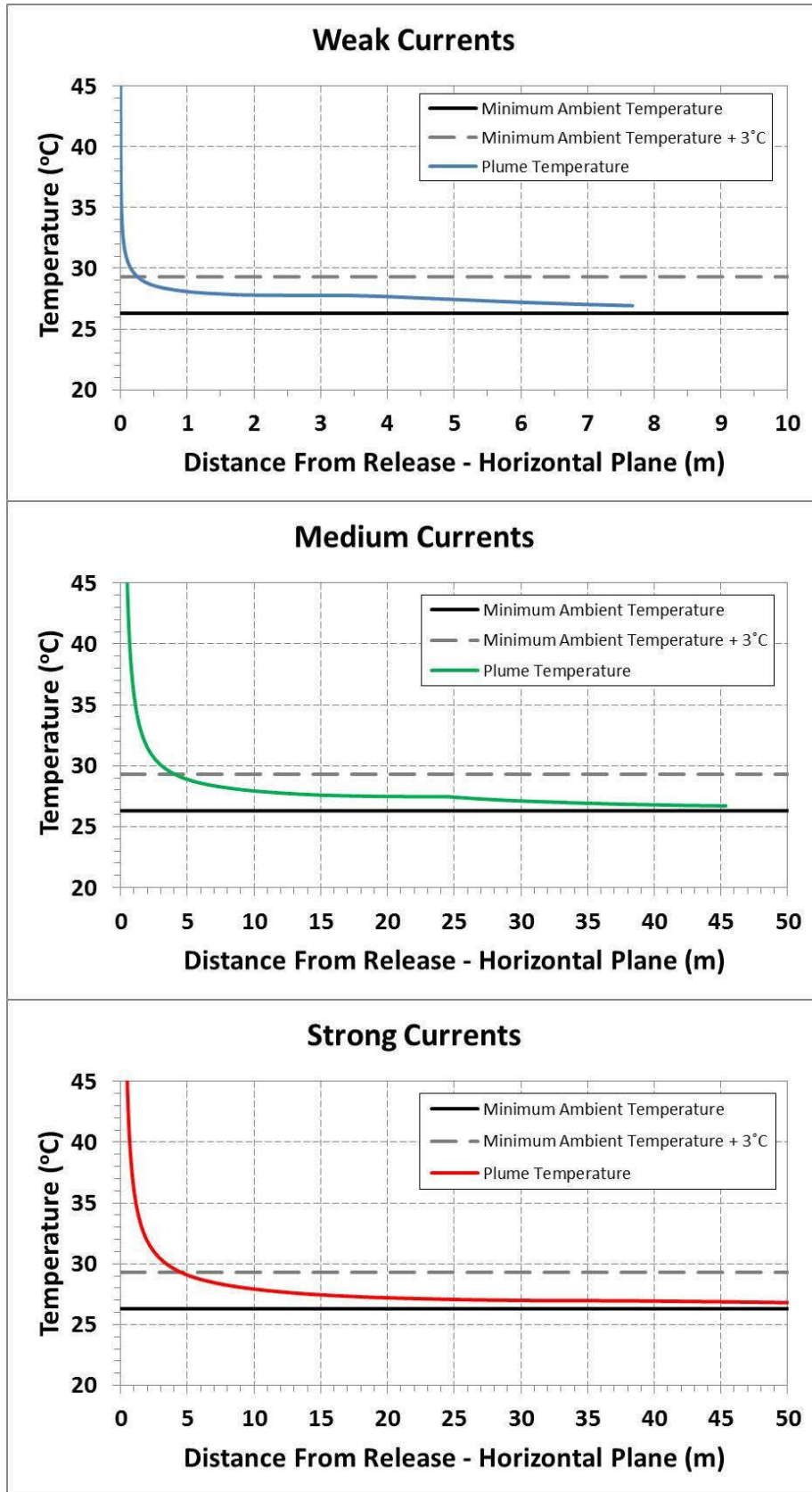
Figure 38 Predicted change in cooling water plume temperature as a function of distance from release location under weak, medium and strong current strengths during winter conditions (360,576 m³/d)